Limits on Dione's Activity using Cassini/CIRS data

Carly J.A. Howett[1], John R. Spencer[1], Terry Hurford[2], Anne Verbiscer[3] and Marcia Segura[2]

[1] Southwest Research Institute, Boulder, CO 80302, USA.
[2] Godard Space Flight Center, Maryland, USA.
[3] University of Virginia, Virginia, USA

Corresponding author: Carly J.A. Howett (howett@boulder.swri.edu) †

† Contact Information of Corresponding Author
1050 Walnut Street, Suite 300
Boulder, Colorado, 80302, USA
Telephone Number: +1 720 240 0120
Fax Number: +1 303-546-9687

Key Points:

- We use Cassini CIRS data to map Dione's nighttime temperature to look for evidence of surface activity.
- Observed temperatures are consistent with passive emission, and no evidence for hotspots (indicative of activity) is observed.
- We derive a temperature upper limits and limits of endogenic emission for 50, 100 and 200 km^2 hotspots.

Index Terms
6280 Saturnian satellites
5418 Heat flow
5464 Remote sensing
5470 Surface materials and properties
5422 Ices

Index Keywords
Dione; Activity; CIRS

Plain Language Summary

We use data from NASA's Cassini spacecraft to map the nighttime surface temperature of one of its large icy moons Dione. These maps show no evidence of small very hot regions, which (if present) would provide evidence of activity on Dione. Instead the surface temperatures we do see are comparable with those we would expect to see on Dione if it were inactive. So we find no evidence for activity on Dione in this study. However, it is possible that very small regions of high surface temperatures would not be detected in this work. We use the observed surface temperatures to define how hot a small region (50, 100 or 200 km^2) could be, and remain undetected. The results show such a region would have a mean temperature of 117.1±47.2 K (-249 F), 104.8±27.7 K (-272 F) and 95.4±19.5 K (-288 F) for a 50, 100 and 200 km2 hotspot respectively, corresponding to endogenic emission of 1.07, 0.68 and 0.47 GW.

Abstract

We use nighttime Cassini Composite Infrared Spectrometer (CIRS) data to look for discrete regions of elevated nighttime temperatures indicative of endogenic activity on Dione's surface. This is achieved by producing low- and mid-latitudes (less than 60°) maps of Dione's nighttime surface temperature, derived from 10 to 1100 cm^{-1} CIRS data. The surface temperatures observed do not show evidence of any small discrete regions of elevated nighttime temperatures, and are comparable to temperatures predicted by a passive thermophysical model of Dione's surface. Thus, we conclude that no evidence for activity exists on Dione at mid- to low-latitudes. Using the derived surface temperature maps we set upper-limits for the temperature at which a 50, 100 or 200 km^2 hotspot would remain undetected by this study. We find the mean temperature of such a hotspot would be 117.1±47.2 K (-249 F), 104.8±27.7 K (-272 F) and 95.4±19.5 K (-288 F) for a 50, 100 and 200 km^2 hotspot respectively, corresponding to endogenic emission of 1.07, 0.68 and 0.47 GW.

1 Introduction

There have been hints that Dione may be active from a number of sources, but none of them have been able to definitively prove activity. We know Dione's surface is one of the most geologically complex of all the mid-sized satellites (only beaten by active Enceladus). It has fresh fractures, evidence of extensive faulting and resurfacing (Smith et al., 1982; Roatsch et al., 2008, 2009; Schenk and Moore 2009), but nothing that conclusively proves Dione is currently active.

Plasma flow from Dione was detected by Cassini's Plasma Spectrometer (CAPS), possibly indicating outgassing perhaps from recent geological activity (Burch et al., 2007). Specifically a double peaked ''butterfly'' pitch-angle distribution was observed, which could be explained by two plasma streams originating separately from Tethys and Dione, which form plasma tori at the locations of their orbits. However, Rymer et al. (2008) argue that this signature could simply be caused by electron recirculation within Saturn's magnetosphere. Observations made by Cassini's Visual Infrared Mapping Spectrometer (VIMS) taken in 2004 show a tentative detection of a particle halo around Dione (Clark et al., 2008). If it exists, the halo of methane and water ice

could have been ejected from endogenic activity on Dione. However, such a halo has not been observed again.

Perturbations in Dione's magnetic field detected by Cassini's Magnetometer were consistent with the presence of an exosphere around Dione (Simon et al., 2011). Cassini's Ion and Neutral Mass Spectrometer (INMS) also found evidence of a tenuous carbon dioxide and oxygen exosphere at both Dione and Rhea (Teolis et al., 2012; Teolis and Waite 2016). While the Cassini Plasma Spectrometer (CAPS) detected O2+ pickup ions at Dione, further confirming the presence of an exosphere (Tokar et al. 2012). The source of Dione's exosphere is unclear: activity is one possibility, but surface interactions with Saturn's magnetosphere and/or solar illumination are also possible mechanisms.

Searches for plume activity from Dione have been unsuccessful (Buratti et al., 2011). VIMS observations of Dione's at 2.02 μm at large solar phase angles revealed no forward scattering peaks, which would have been indicative of plume activity. In the same study a visual inspection of images taken of Dione by Cassini's Imaging Science Subsystem (ISS) was made, and also revealed no evidence for plume activity. An upper limit on water vapor column density was produced 1.29×10^{14} to 1.68×10^{15} cm^{-2}; which is two orders of magnitude lower than on active Enceladus (Buratti et al., 2011). A follow up study by Buratti et al. (2018) used high solar phase angle Cassini VIMS observations, inspection of 2.65 μm VIMS images, and stellar occulations from Cassini's Ultraviolet Imaging Spectrometer (UVIS) to search for evidence of plumes from Dione. They found no evidence for even low-level activity on Dione (or Tethys).

The activity on Enceladus was discovered early in the Cassini mission (Dougherty et al., 2006; Hansen et al., 2006; Porco et al., 2006; Spahn et al., 2006; Spencer et al., 2006). Enceladus' activity is concentrated at its south pole, along four fractures nicknamed "tiger stripes". The temperature along these stripes is well above the ~70 K background surface temperature: 177 to 198 K (Spencer et al., 2011; Goguen et al. 2013). Such activity would not have gone unnoticed on Dione! So it is not Enceladus-level activity that this work seeks to discover, but small-scale, subtle activity, perhaps barely warmer than the surroundings.

2 Data Analysis

All the data used in this work were taken by Cassini's Composite Infrared Spectrometer (CIRS), (Flasar et al., 2004). CIRS is a Fourier transform spectrometer with three focal planes, covering 10 to 1400 cm^{-1} (7.1 to 1000 microns). Low wavenumbers 10 to 600 cm^{-1} (16.7 to 1000 microns) are detected by focal plane 1 (FP1), which has a spatial resolution of 3.9 mrad. While wavenumbers between 600 to 1100 cm^{-1} (9.1 to 16.7 microns) and 1100 to 1400 cm^{-1} (7.1 to 9.1 microns) are detected by focal planes 3 and 4 respectively (FP3 and FP4). These two focal planes each have a row of ten detectors, each of which has a 0.273 by 0.273 mrad field of view. The wavelength range of FP1 makes it sensitive to both daytime (>65 K) and nighttime (<65 K) surface temperatures of the icy Saturnian satellites, whilst FP3 is only sensitive to daytime temperatures on most of the satellites (>65 K). The sensitivity of FP4 to surface temperatures of the icy Saturnian satellites is too low to be of use, with the exception of Iapetus and the warm active regions on Enceladus (>110 K).

In order to search for low-levels of endogenic activity on Dione we concentrate on nighttime observations, since any warm endogenic heat signatures should be easier to observe against

cooler nighttime temperatures than warmer daytime ones. Nighttime temperatures on Dione range between ~55 to 70 K (Howett et al., 2010), which is well within the sensitivity of FP1. However, since active regions are expected to be warmer than these background temperatures it maybe possible to detect activity with FP3 too. Furthermore, FP3's spatial resolution is almost an order of magnitude better than FP1, so it is better suited to finding small-scale activity (the most likely type, as it is expected that large-scale active regions would have been already discovered). So observations of Dione made by both FP1 and FP3 data are the focus of this work.

Dedicated scans of Dione are the focus of this work, since they provide systematic coverage of a large surface region; Table S1 details the specific observations analyzed. FP1 observation span almost the length of the Cassini mission at Saturn, while the FP3 observations are concentrated towards the end of the mission (2010-2015). This is because initially FP1 was used to make nighttime observations of icy satellites since it is more sensitive than FP3 to such temperatures. However, later in the mission when there was increased interest in searching for activity on Dione FP3 observations were made too, since its better spatial resolution made it better suited to look for small-scale high temperature features. We limit the data to those with an emission angle of <60°, since observations at high emission angles preferentially observe high elevation regions, the temperature of which may not be representative of the bulk surface temperature.

We use the same analysis technique for each observation. First the observations are gridded into 0.5° by 0.5° latitude/longitude bins. When a bin is covered by a single observation then the radiance of that observation is assumed for the bin, but when a bin is observed by multiple observations then the mean radiance of those observations is assumed. Then, the temperature of each bin was determined by finding the best-fitting blackbody temperature curve to the bin's radiance using IDL's amoeba algorithm (a downhill simplex method based on the work of Nelder and Mead, 1965), on the assumption that the surface emits as a blackbody. The noise on the derived surfaces temperatures is derived using a two-step Monte Carlo technique: first a synthetic noise with a comparable magnitude to the observed noise is created and added to the previously determined best fitting blackbody curve. Then this spectrum is fitted by a blackbody emission spectrum. This process is repeated numerous times, and the temperature error estimate is given by the standard deviation of the temperatures whose blackbody emission spectra are best able to fit the created spectra.

The next step was to determine what the expected surface temperatures would be for a given observation. To do this a seasonal 1-D thermal model was used (c.f. Spencer, 1989). The model accounts for the effects of eclipses, radiation from Saturn, heliocentric distance, rotation speed of the target, latitude, local time and subsolar latitude. The albedo and thermal inertia of the surface were set to cover the range of values previously determined by Howett et al. (2014) (Figure S1). However, the maps produced by Howett et al. (2014) did not have global coverage: there are gaps in coverage spanning between 10 and 50° longitude and only latitudes less than ±60° were covered. No attempt was made to increase the latitude coverage of Howett et al. (2014) maps, since information on the thermal properties of Dione's poles are unknown and CIRS observations of Dione's polar regions are sparse. However gaps in longitude were filled to make new albedo and thermal inertia maps by interpolating albedo or thermal inertia across longitudes at a given latitude. The resulting 10°x10° albedo and thermal inertia maps are given in Figure 1 (see below for further discussion of map resolution). A comparison of Figures 1 and S1 show

that the general albedo and thermal inertia trends described by Howett et al. (2014) have been conserved. Specifically, Dione's trailing hemisphere is darker than its leading one (consistent with the literature, e.g. Schenk et al, 2011; Clark et al., 2008; Stephan et al., 2010; Scipioni et al., 2013) and a high thermal inertia region is located at low latitudes on Dione's leading hemisphere (Howett et al., 2014). The errors on the thermal inertia and albedo are the same as Howett et al. (2014), but in regions of interpolation the maximum error of Howett et al. (2014) maps are assumed (i.e. 4 MKS on thermal inertia and 0.12 on albedo). Thermal inertia depends upon the nature of the surface (e.g. grain size, contact between grains and composition). On Dione the most significant change in thermal inertia is linked to modification of contact between grains by high-energy electrons (Howett et al., 2014).

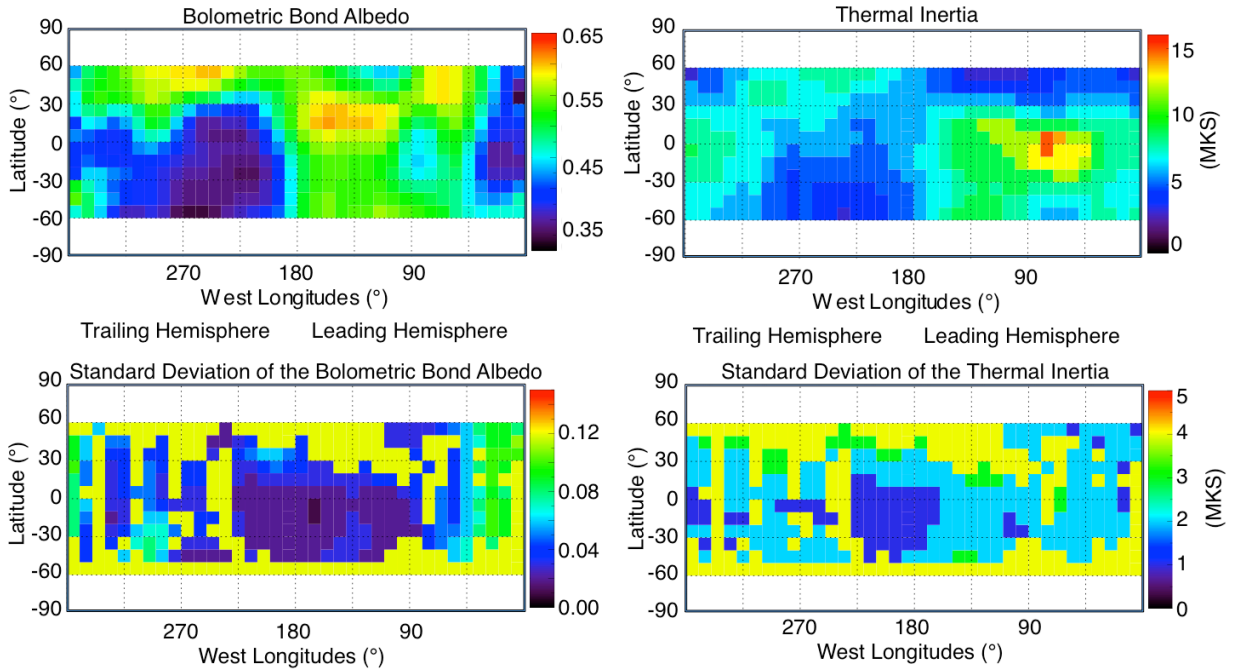

Figure 1 – Maps of thermal inertia and bolometric Bond albedo and their errors in 10° by 10° bins, which are assumed for Dione in this work.

The seasonal model was run for each 10° by 10° longitude and latitude grid point separately, because the local time of eclipse ingress and egress varies with longitude and insolation varies with latitude. This made the modeling computationally expensive, so it was impractical to run the model for every possible albedo and thermal inertia combination. Therefore, models at a number of albedo and thermal inertias spanning the range of expected values were run (albedos between 0.30 to 0.7, and thermal inertias between 2 and 20 MKS, see Figure S2), and then surface temperatures for intermediate albedo/thermal inertia values were found by interpolating these results. The required albedo and thermal inertia coverage was initially estimated, and then more points added as required to provide the necessary bounds for the interpolated albedo and thermal inertia values.

The temperatures predicted by the seasonal models for each observation epoch are given in the top right-hand panel in Figures 2 and 3. Their error is assumed to be the maximum temperature

difference between the surface temperature predicted by the nominal albedo/thermal inertia and that by the nominal value +/- their uncertainty (middle right panel). This difference is assumed to be the dominant error on the predicted temperatures. The errors are shown in the same latitude and longitude resolution as the original thermophysical property maps (i.e. 10° by 10°), whereas the surface temperatures have been interpolated to the same resolution as the maps of observed temperature (0.5° by 0.5°). Surface temperatures are expected to vary smoothly across Dione, but the errors do not (especially since in some regions there is a sharp increase in their value where we moved from derived values to interpolated ones). So it makes sense to interpolate the expected surface temperatures, to direct comparison between the predicted and observed temperatures, but not do the same with the predicted model errors.

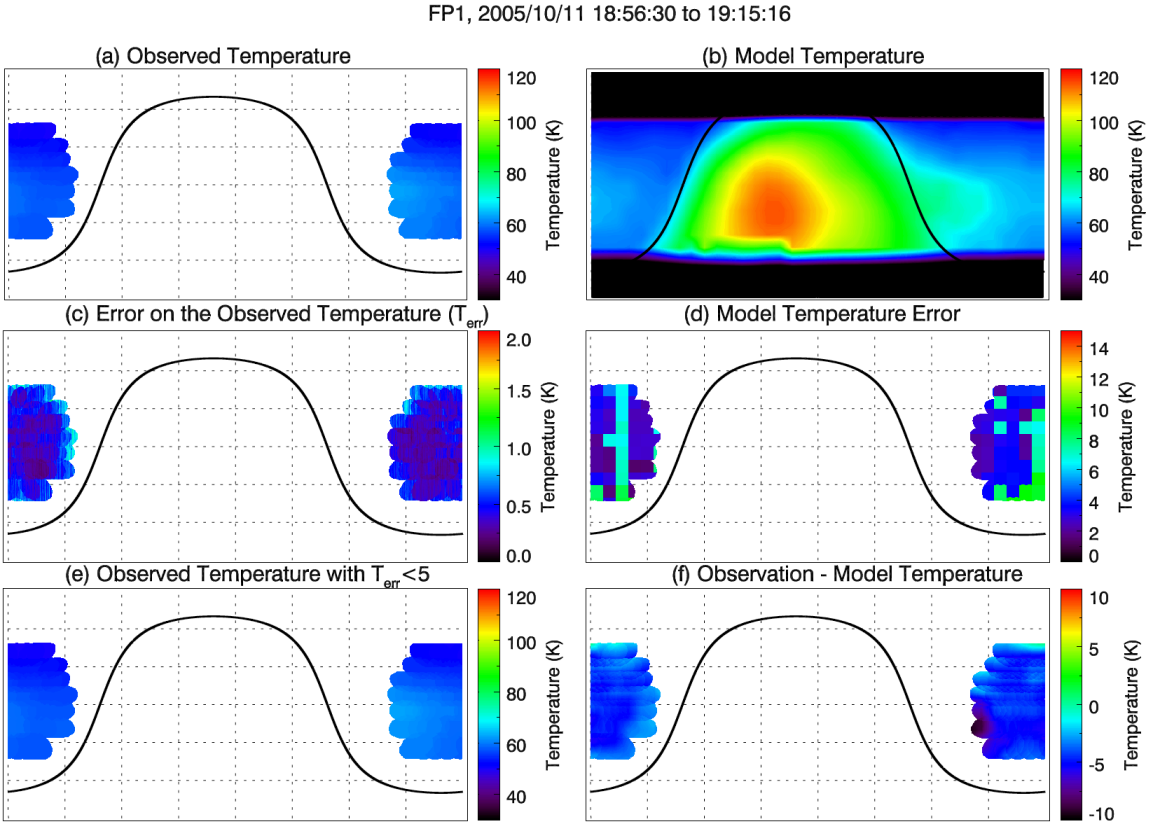

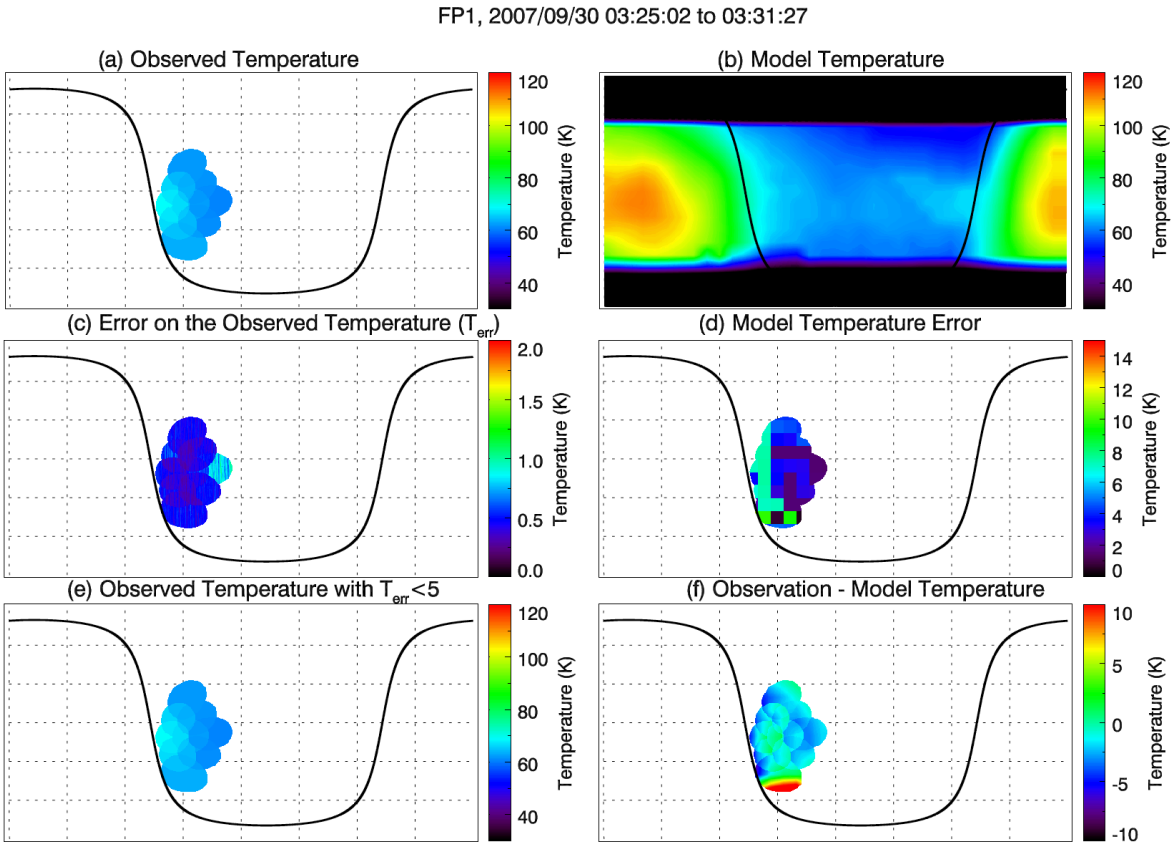
FP1, 2007/09/30 03:25:02 to 03:31:27
(a) Observed Temperature
(b) Model Temperature
(c) Error on the Observed Temperature (T_err)
(d) Model Temperature Error
(e) Observed Temperature with T_err<5
(f) Observation - Model Temperature
Temperature (K)

205

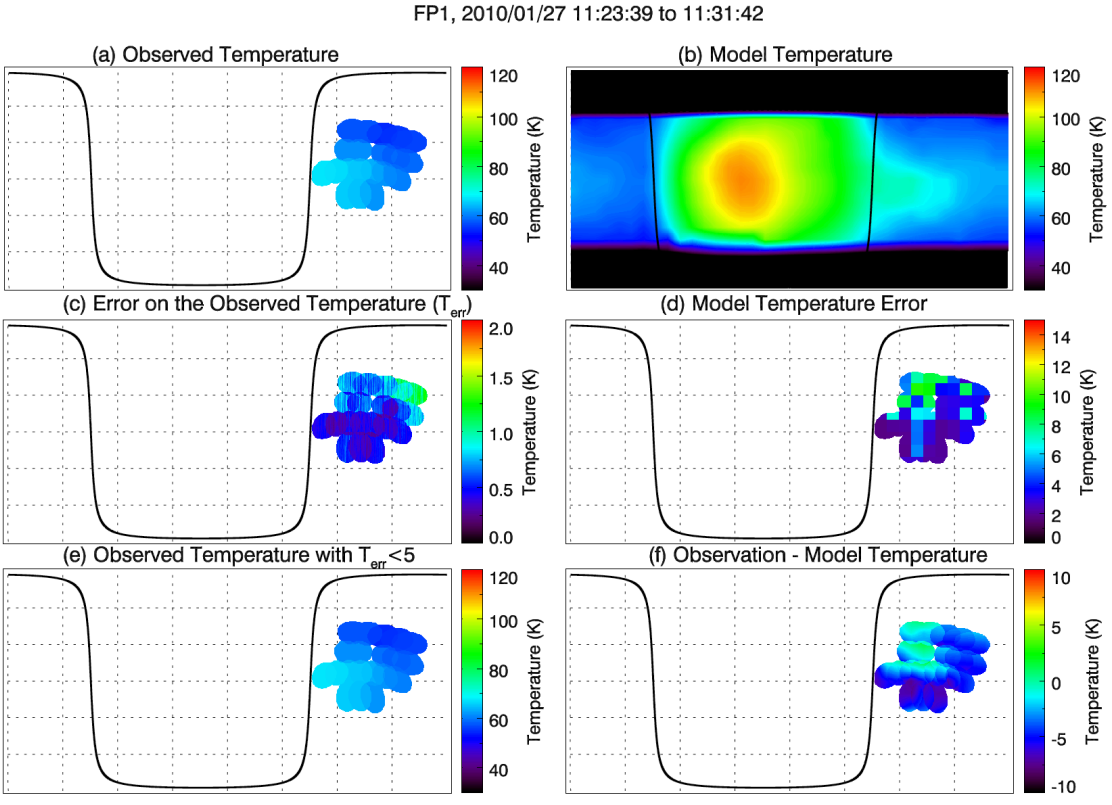
FP1, 2010/01/27 11:23:39 to 11:31:42
(a) Observed Temperature
(b) Model Temperature
(c) Error on the Observed Temperature (T_err)
(d) Model Temperature Error
(e) Observed Temperature with T_err<5
(f) Observation - Model Temperature
Temperature (K)

206

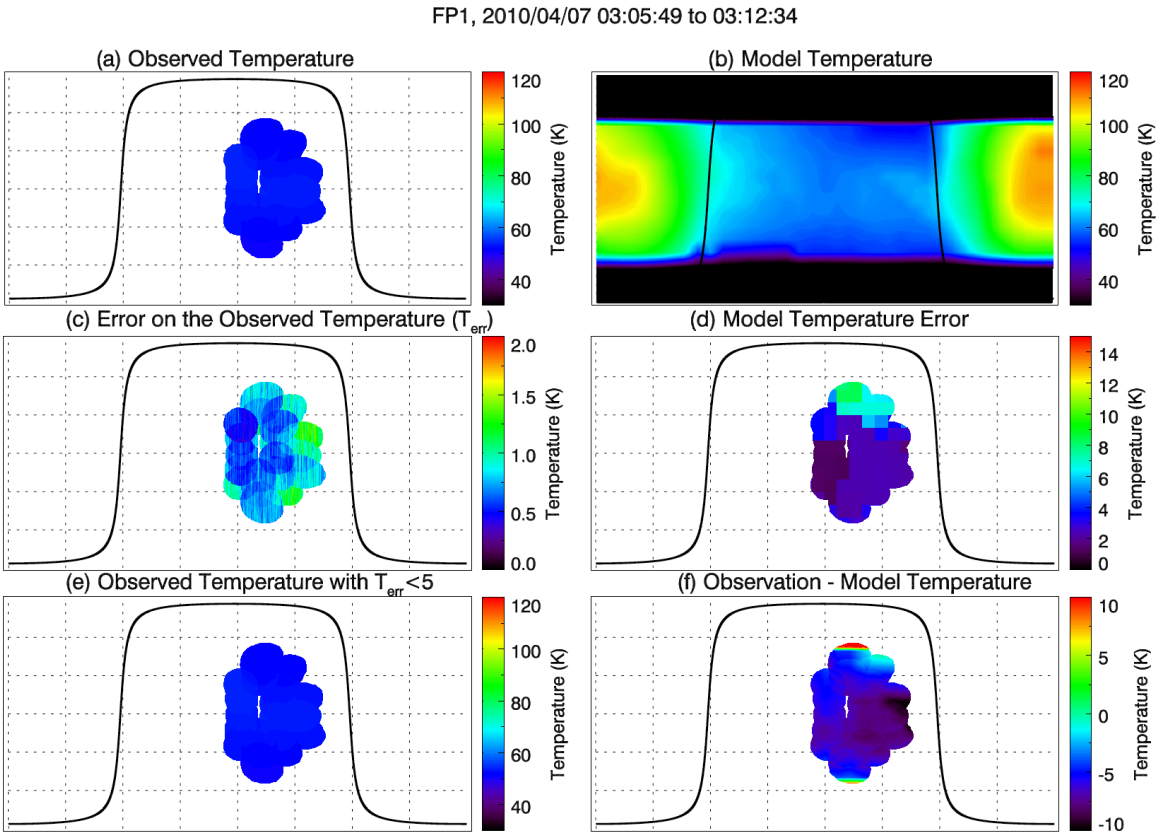
FP1, 2010/04/07 03:05:49 to 03:12:34
(a) Observed Temperature
(b) Model Temperature
(c) Error on the Observed Temperature (T_err)
(d) Model Temperature Error
(e) Observed Temperature with T_err<5
(f) Observation - Model Temperature
Temperature (K)

207

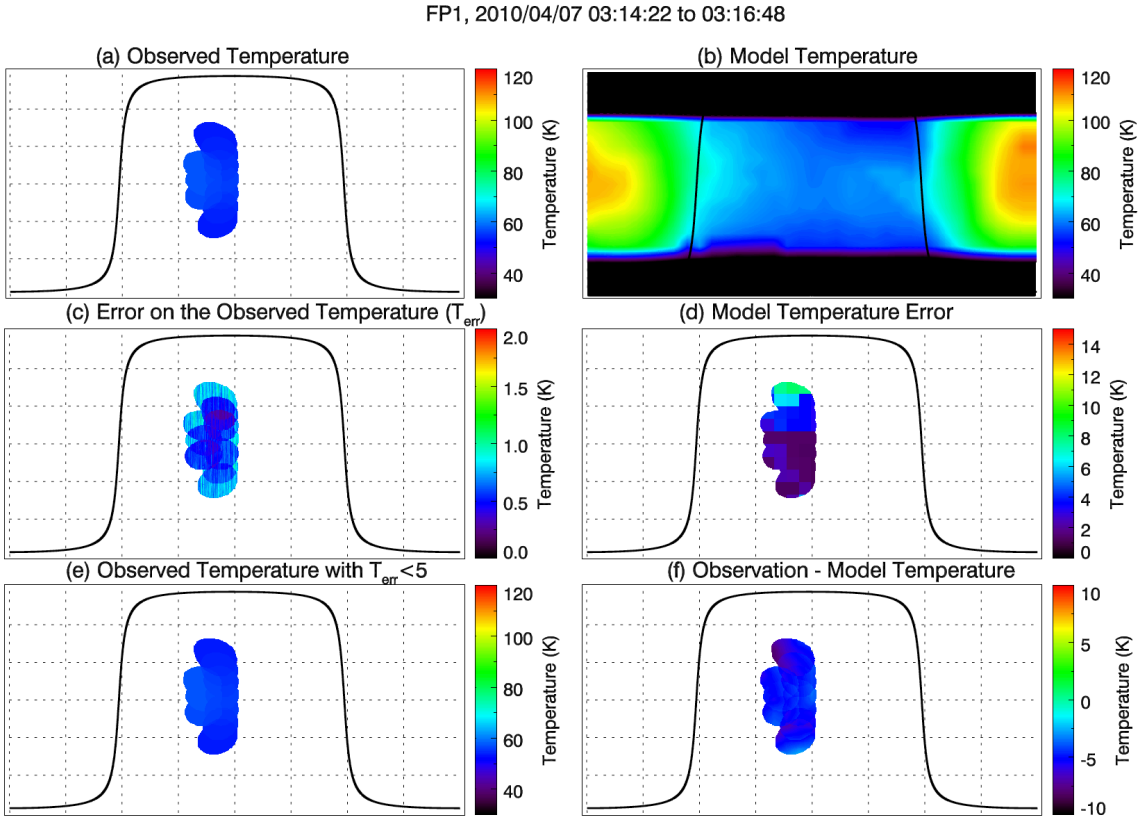
FP1, 2010/04/07 03:14:22 to 03:16:48
(a) Observed Temperature
(b) Model Temperature
(c) Error on the Observed Temperature (T_err)
(d) Model Temperature Error
(e) Observed Temperature with T_err<5
(f) Observation - Model Temperature
Temperature (K)

208

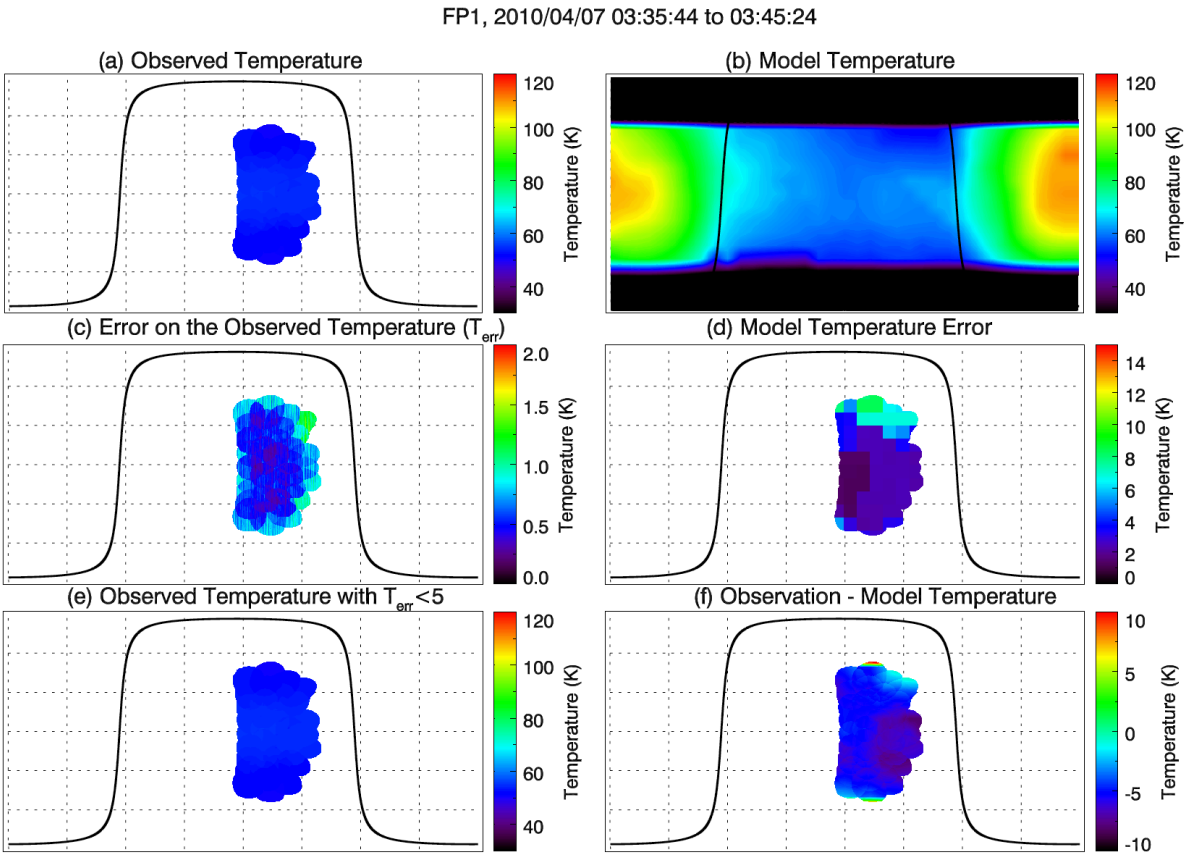
FP1, 2010/04/07 03:35:44 to 03:45:24
(a) Observed Temperature
(b) Model Temperature
(c) Error on the Observed Temperature (T_err)
(d) Model Temperature Error
(e) Observed Temperature with T_err<5
(f) Observation - Model Temperature
Temperature (K)

209

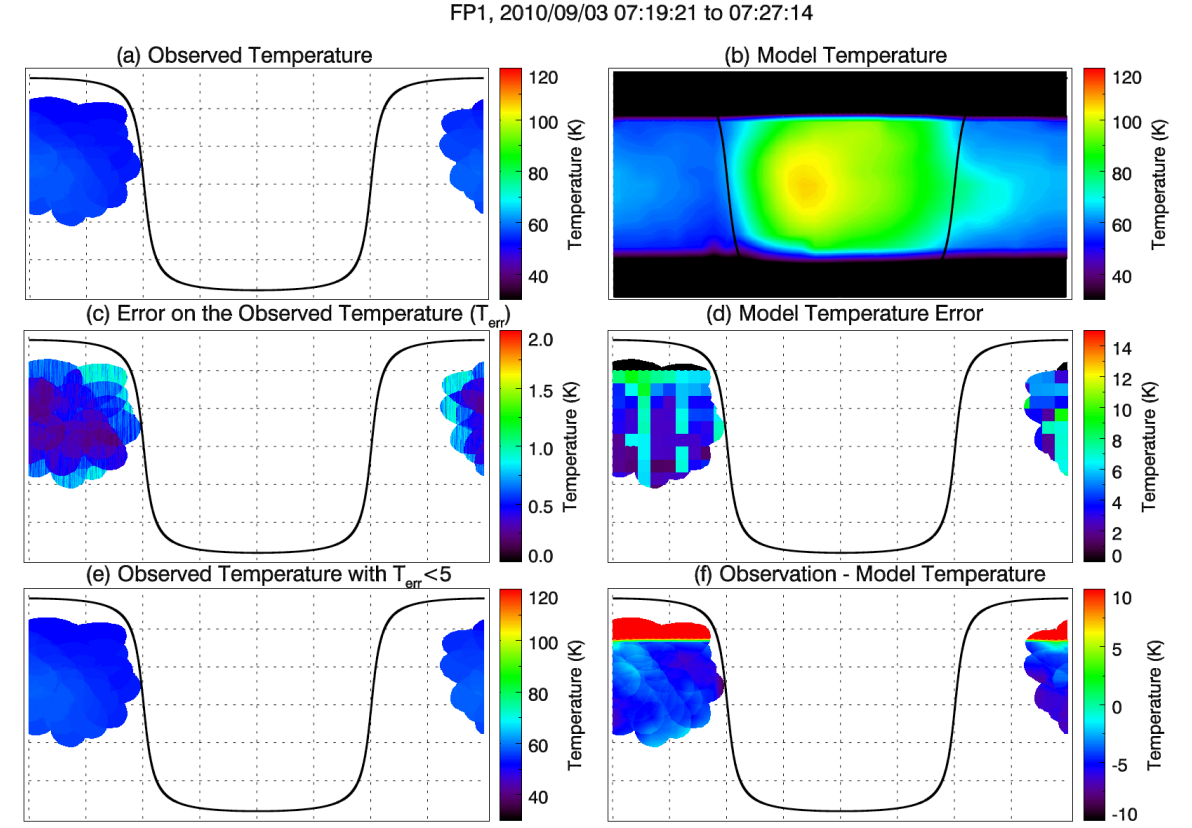
FP1, 2010/09/03 07:19:21 to 07:27:14
(a) Observed Temperature
(b) Model Temperature
(c) Error on the Observed Temperature (T_err)
(d) Model Temperature Error
(e) Observed Temperature with T_err<5
(f) Observation - Model Temperature
Temperature (K)

210

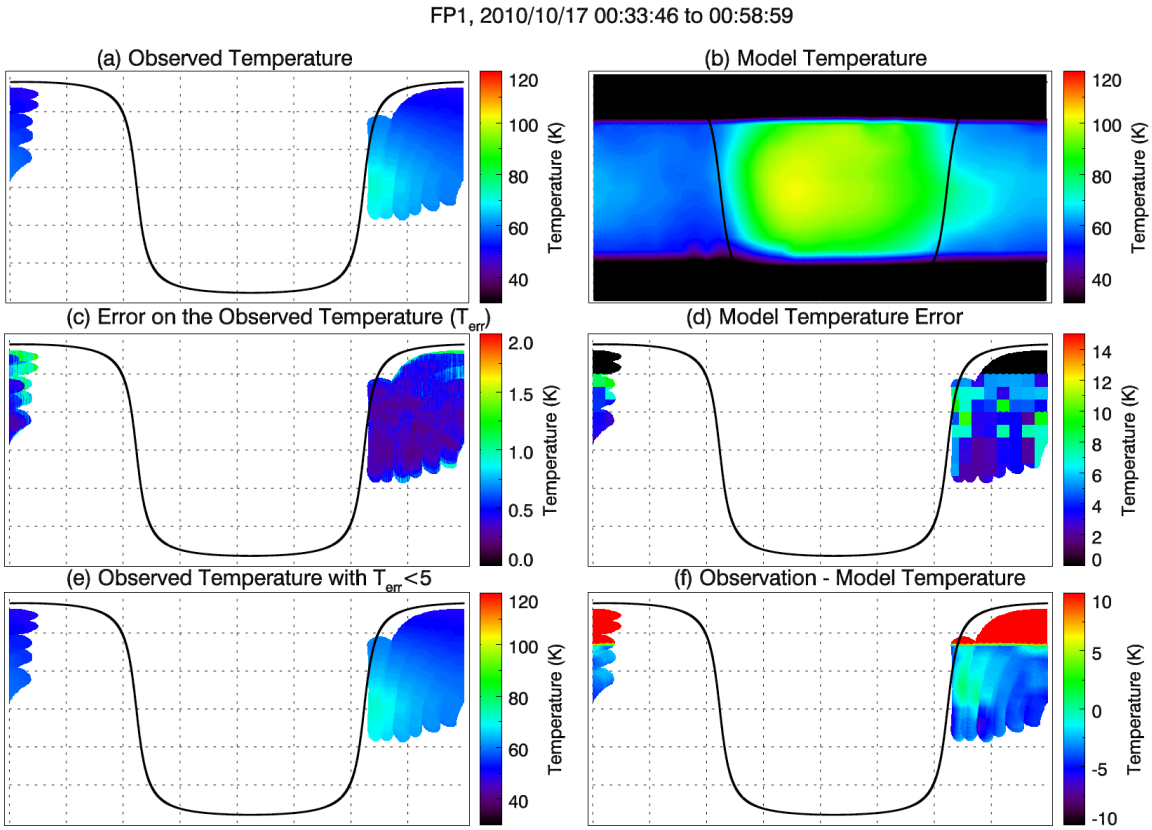
FP1, 2010/10/17 00:33:46 to 00:58:59
(a) Observed Temperature
(b) Model Temperature
(c) Error on the Observed Temperature (T_err)
(d) Model Temperature Error
(e) Observed Temperature with T_err<5
(f) Observation - Model Temperature
Temperature (K)

211

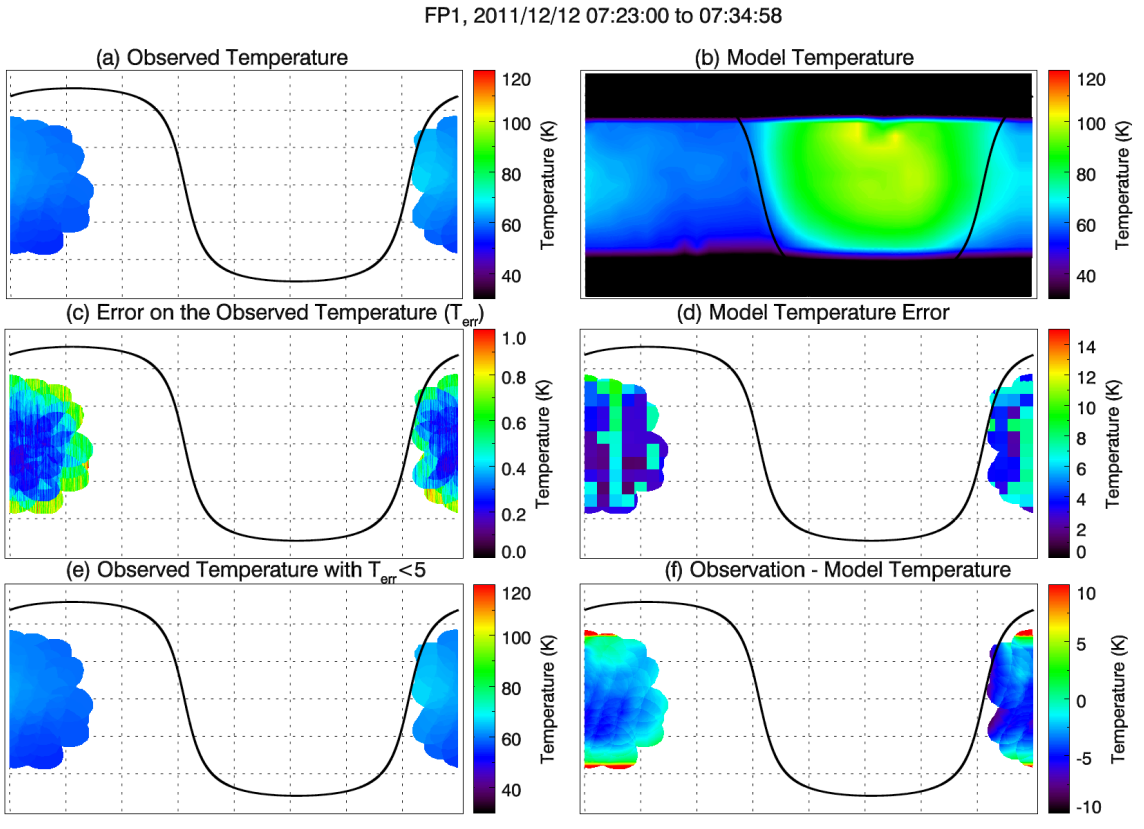
FP1, 2011/12/12 07:23:00 to 07:34:58
(a) Observed Temperature
(b) Model Temperature
(c) Error on the Observed Temperature (T_err)
(d) Model Temperature Error
(e) Observed Temperature with T_err<5
(f) Observation - Model Temperature
Temperature (K)

212

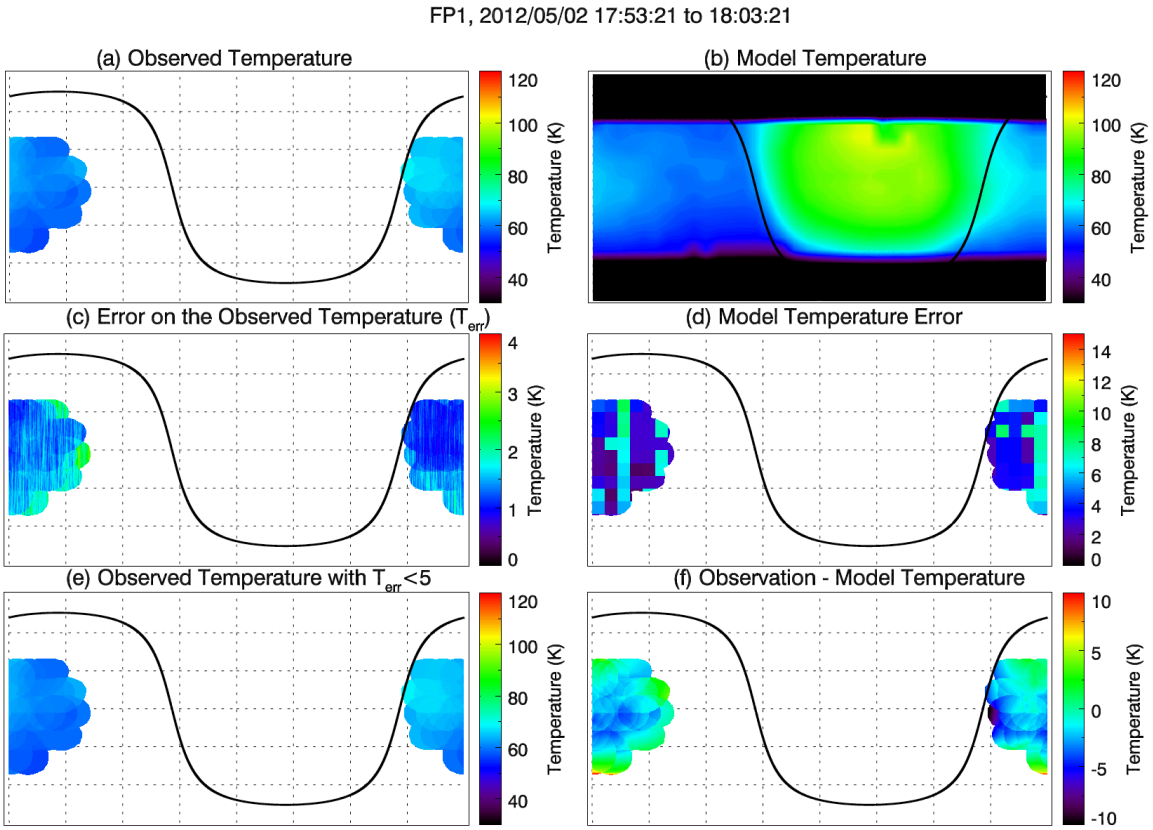
FP1, 2012/05/02 17:53:21 to 18:03:21
(a) Observed Temperature
(b) Model Temperature
(c) Error on the Observed Temperature (T_err)
(d) Model Temperature Error
(e) Observed Temperature with T_err<5
(f) Observation - Model Temperature
Temperature (K)

213

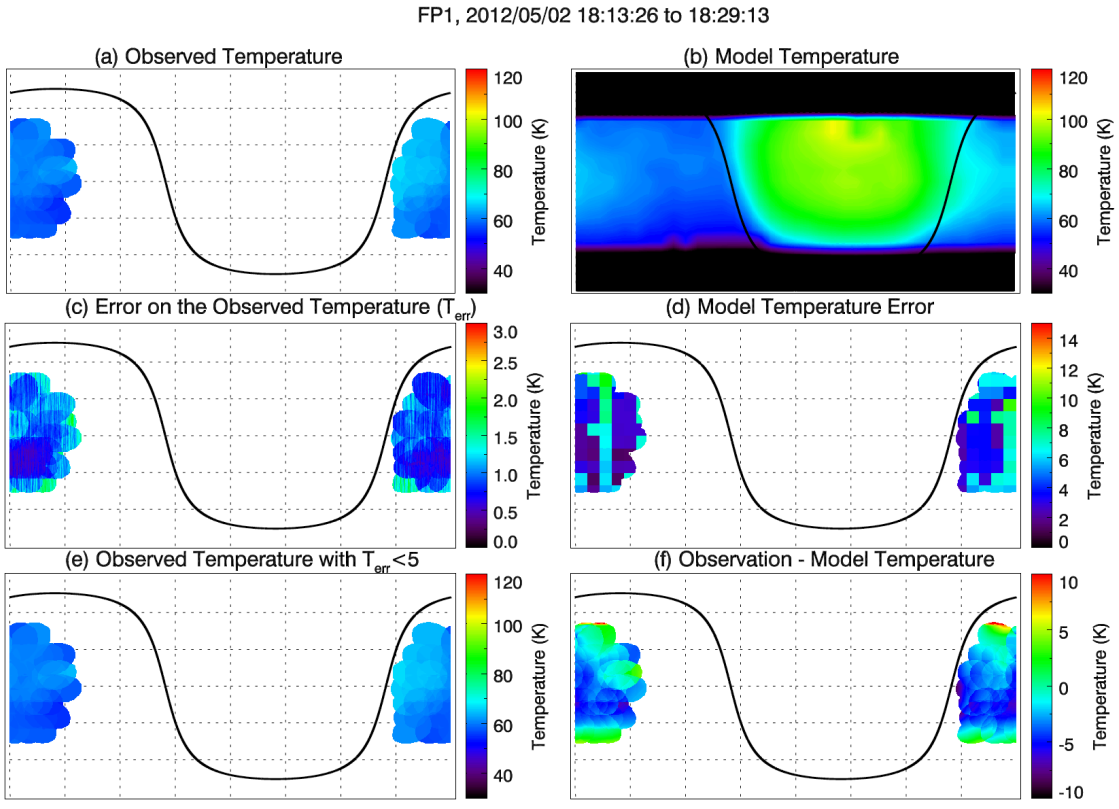
FP1, 2012/05/02 18:13:26 to 18:29:13
(a) Observed Temperature
(b) Model Temperature
(c) Error on the Observed Temperature (T_err)
(d) Model Temperature Error
(e) Observed Temperature with T_err<5
(f) Observation - Model Temperature
Temperature (K)

214

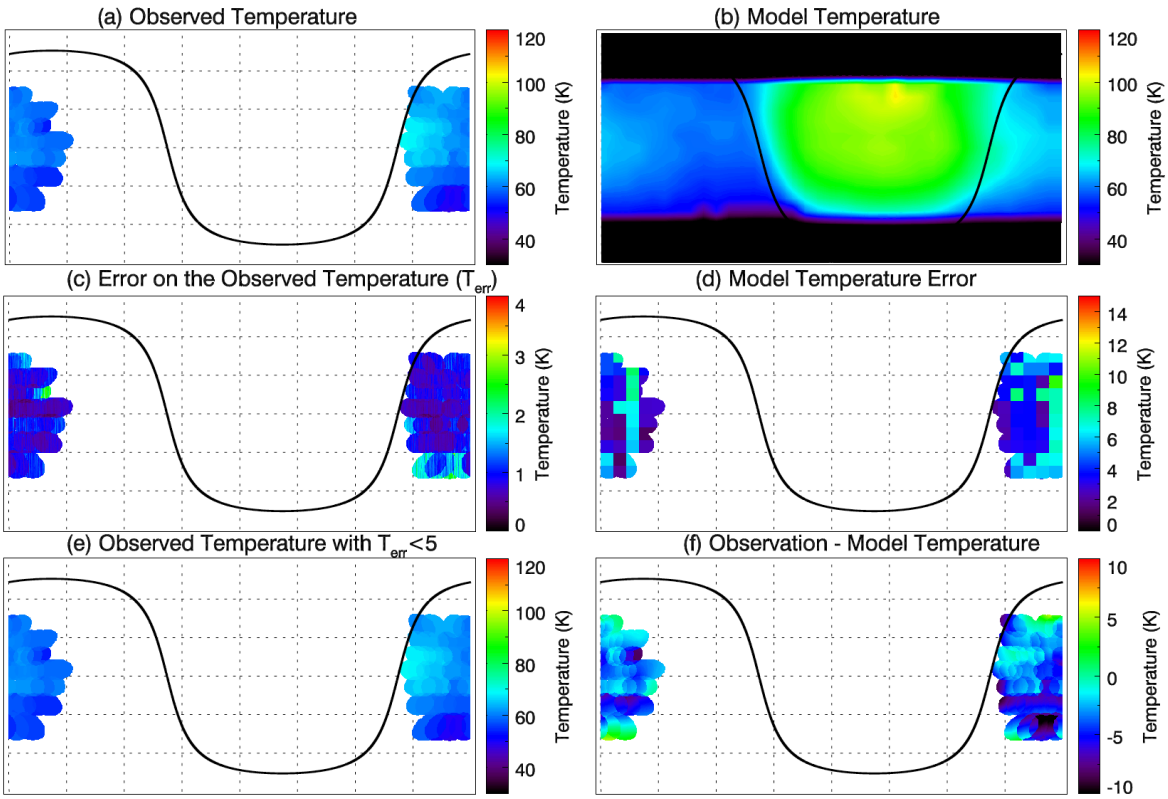
FP1, 2012/05/02 18:49:51 to 19:10:26
(a) Observed Temperature
(b) Model Temperature
(c) Error on the Observed Temperature (T_err)
(d) Model Temperature Error
(e) Observed Temperature with T_err<5
(f) Observation - Model Temperature
Temperature (K)

215

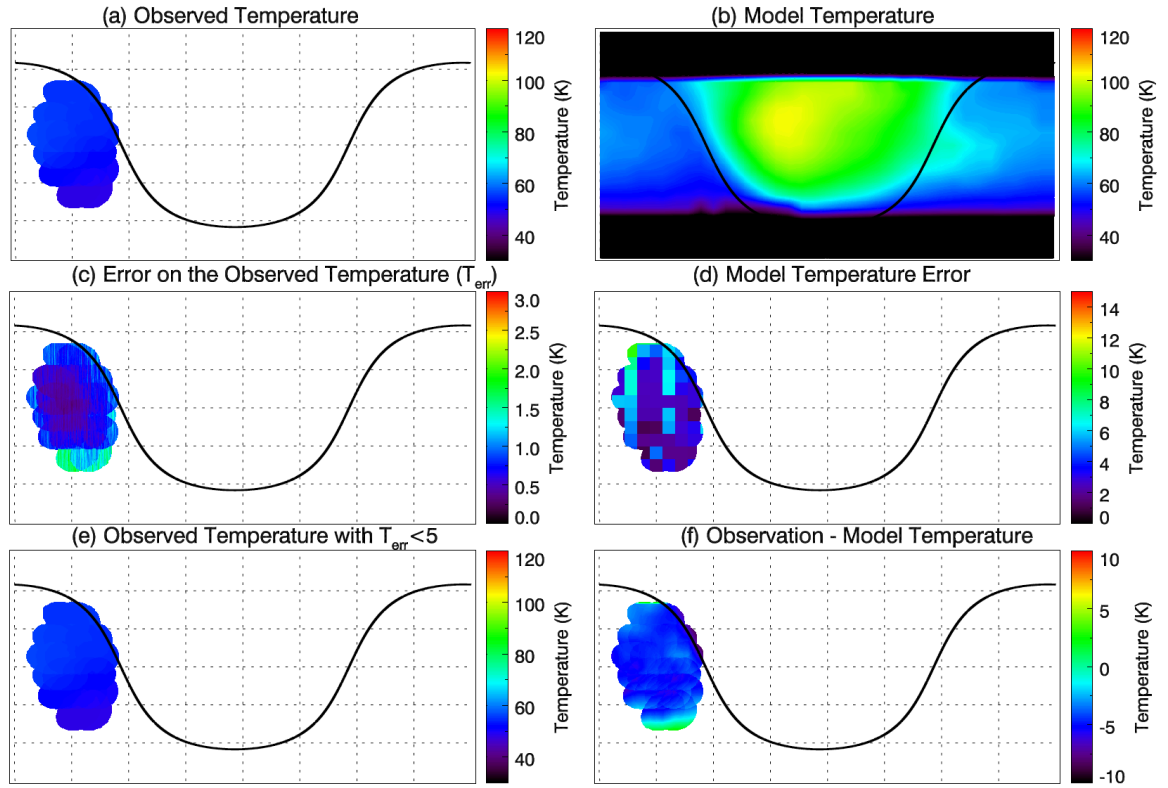
FP1, 2015/07/26 23:39:48 to 23:52:09
(a) Observed Temperature
(b) Model Temperature
(c) Error on the Observed Temperature (T_err)
(d) Model Temperature Error
(e) Observed Temperature with T_err<5
(f) Observation - Model Temperature
Temperature (K)

216

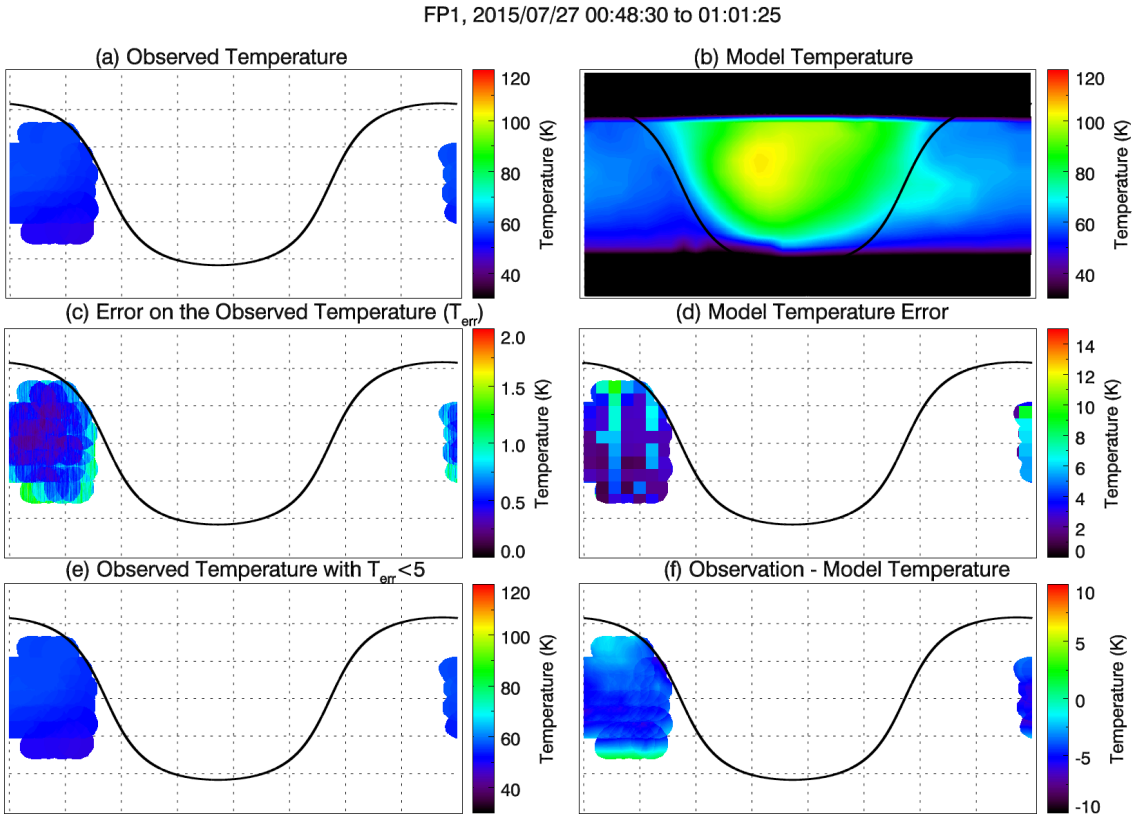
FP1, 2015/07/27 00:48:30 to 01:01:25
(a) Observed Temperature
(b) Model Temperature
(c) Error on the Observed Temperature (T_err)
(d) Model Temperature Error
(e) Observed Temperature with T_err<5
(f) Observation - Model Temperature
Temperature (K)

217

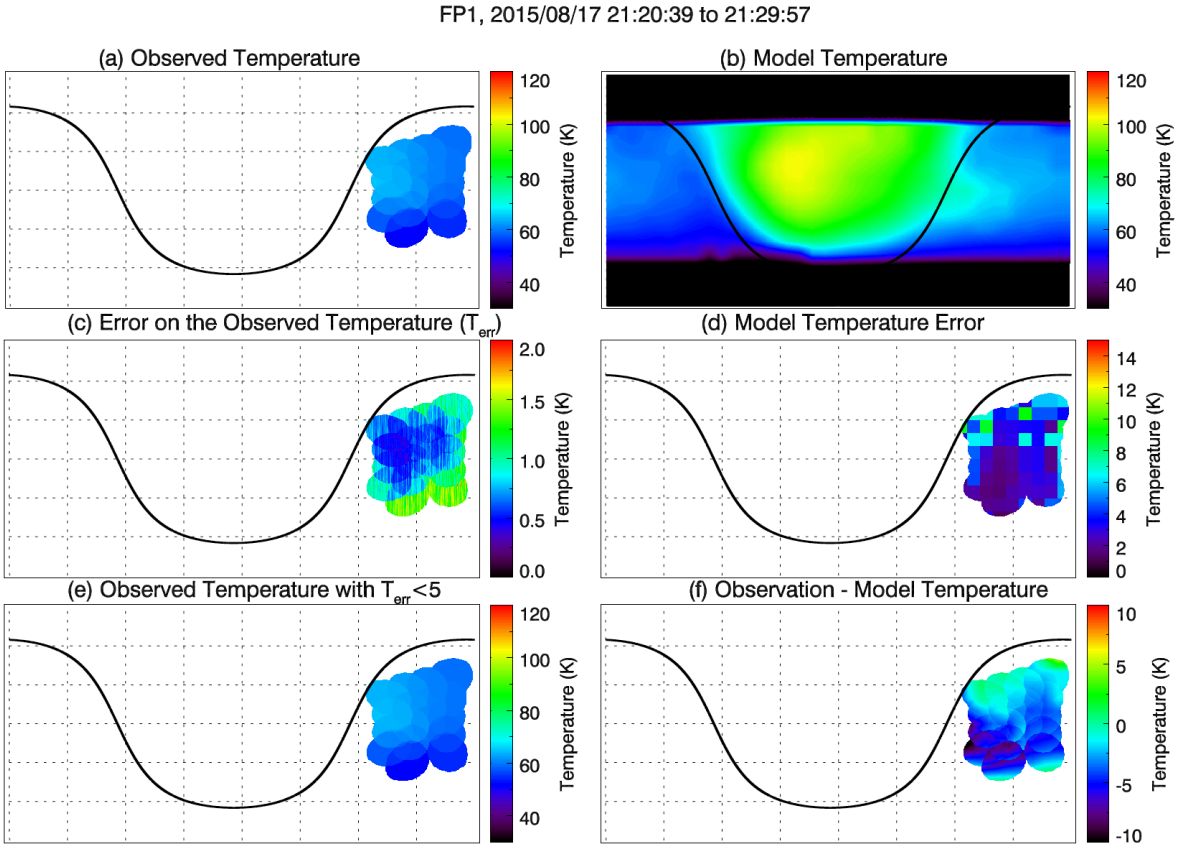
FP1, 2015/08/17 21:20:39 to 21:29:57
(a) Observed Temperature
(b) Model Temperature
(c) Error on the Observed Temperature (T_err)
(d) Model Temperature Error
(e) Observed Temperature with T_err<5
(f) Observation - Model Temperature
Temperature (K)

218

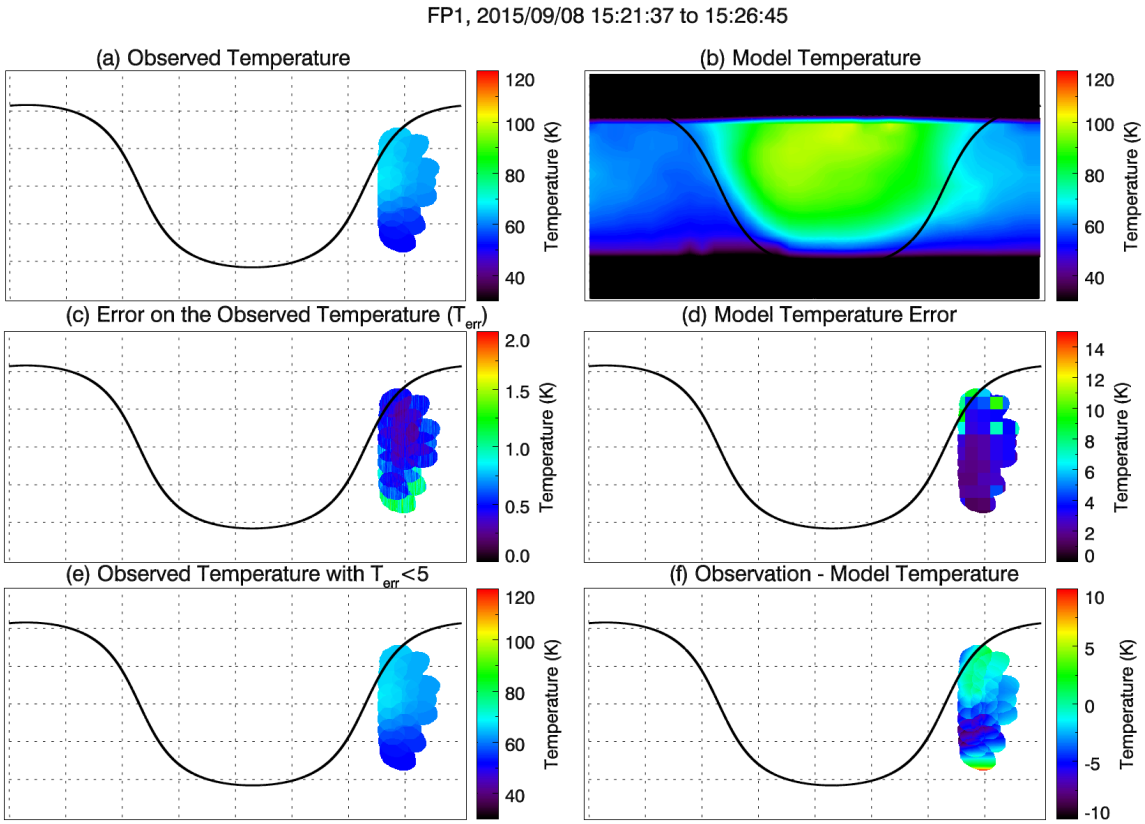
FP1, 2015/09/08 15:21:37 to 15:26:45
(a) Observed Temperature
(b) Model Temperature
(c) Error on the Observed Temperature (T_err)
(d) Model Temperature Error
(e) Observed Temperature with T_err<5
(f) Observation - Model Temperature
Temperature (K)

219

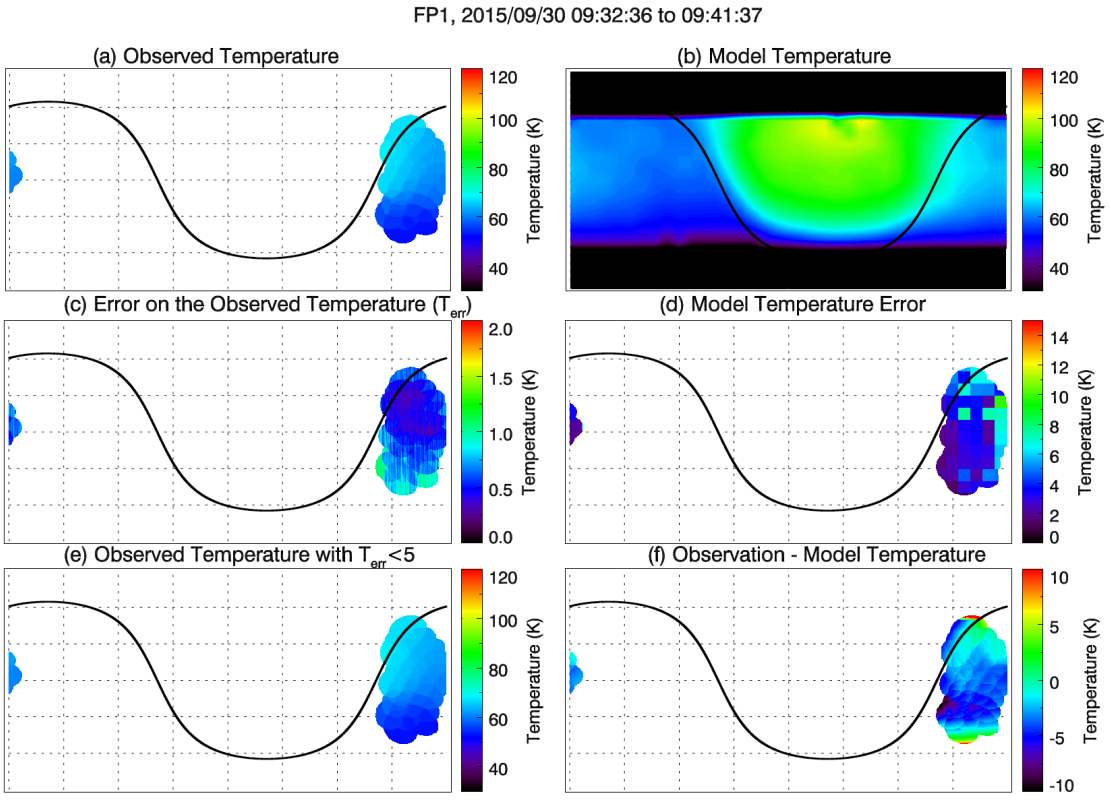
FP1, 2015/09/30 09:32:36 to 09:41:37
(a) Observed Temperature
(b) Model Temperature
(c) Error on the Observed Temperature (T_err)
(d) Model Temperature Error
(e) Observed Temperature with T_err<5
(f) Observation - Model Temperature
Temperature (K)

220

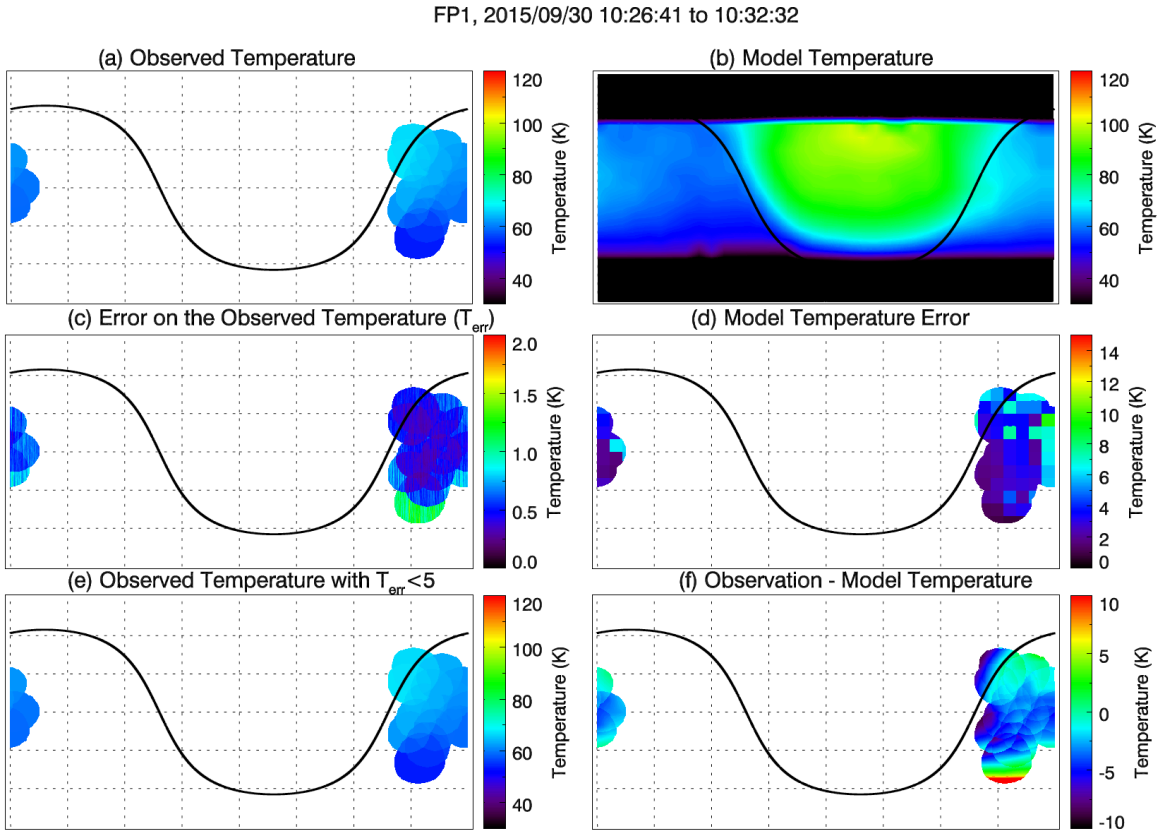

Figure 2 – Maps of the observed and predicted temperature for each observation epoch for FP1 observations. The detector, and start/end time of each observation are given. The left-hand-side show maps of the observed temperature, the error on that observed temperature and only observed temperatures that have an error <5 K. The right-hand-side show predicted model temperatures at the epoch of the observation, with their error. The bottom right-hand-side plot shows the difference in the observed and modeled temperatures for bins where the observed temperatures have an error <5 K. The maps have the same coordinate system as Figure 1, i.e. 360 to 0° W (left to right) longitude and 90° S to 90° N (bottom to top) latitude.

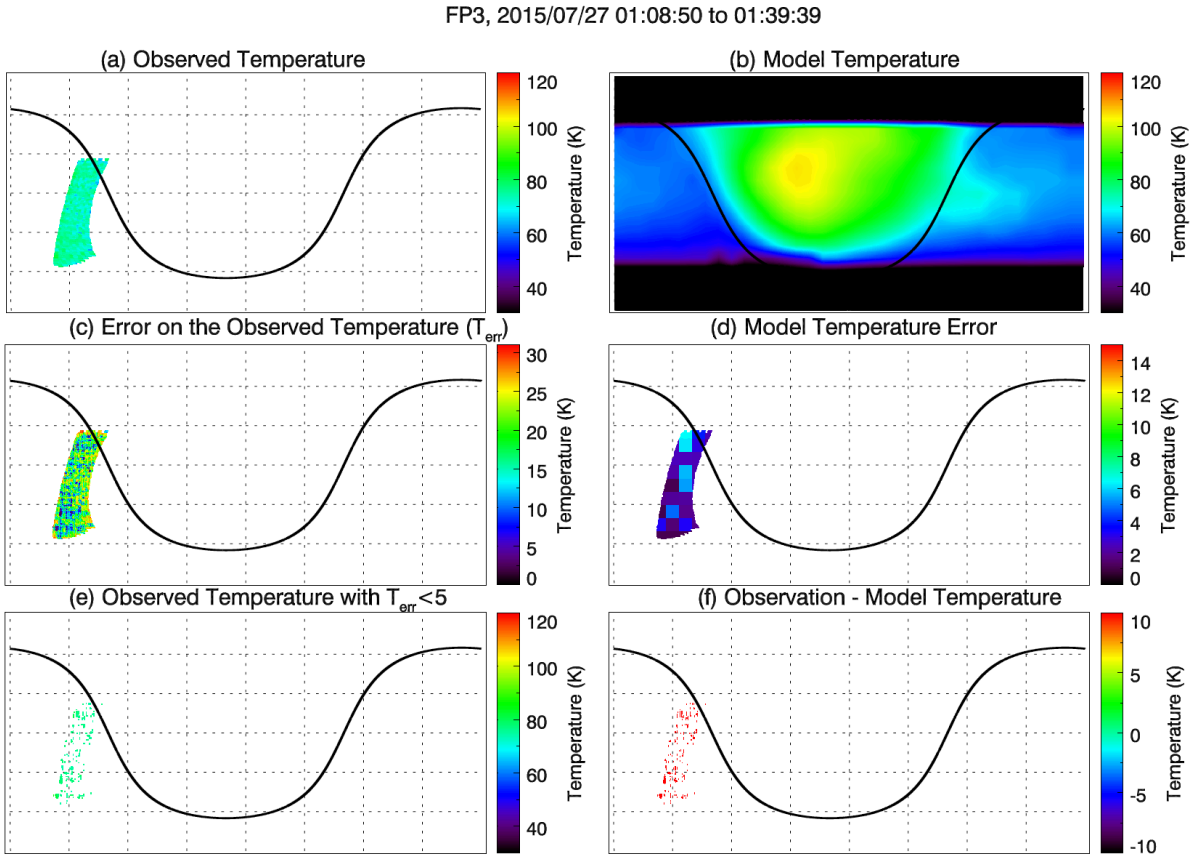
FP3, 2015/07/27 01:08:50 to 01:39:39
(a) Observed Temperature
(b) Model Temperature
(c) Error on the Observed Temperature (T_err)
(d) Model Temperature Error
(e) Observed Temperature with T_err<5
(f) Observation - Model Temperature
Temperature (K)

231

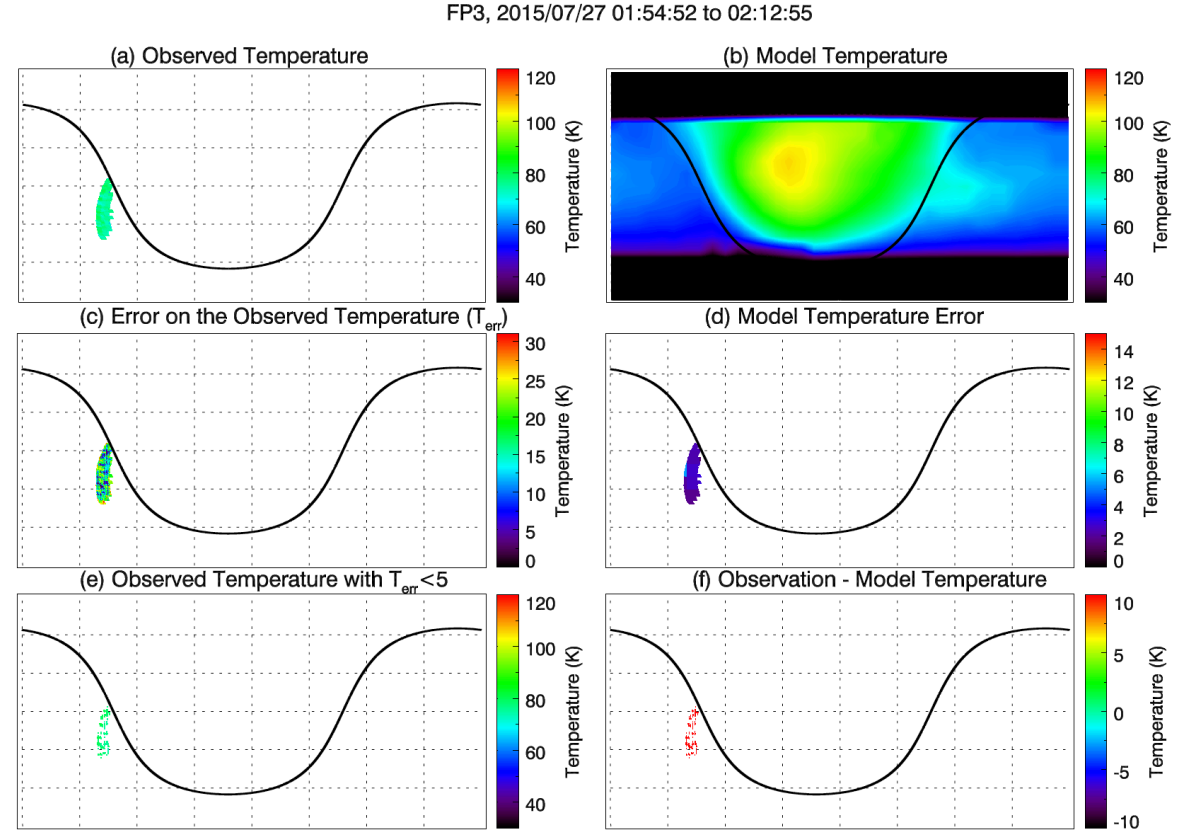
FP3, 2015/07/27 01:54:52 to 02:12:55
(a) Observed Temperature
(b) Model Temperature
(c) Error on the Observed Temperature (T_err)
(d) Model Temperature Error
(e) Observed Temperature with T_err<5
(f) Observation - Model Temperature
Temperature (K)

232

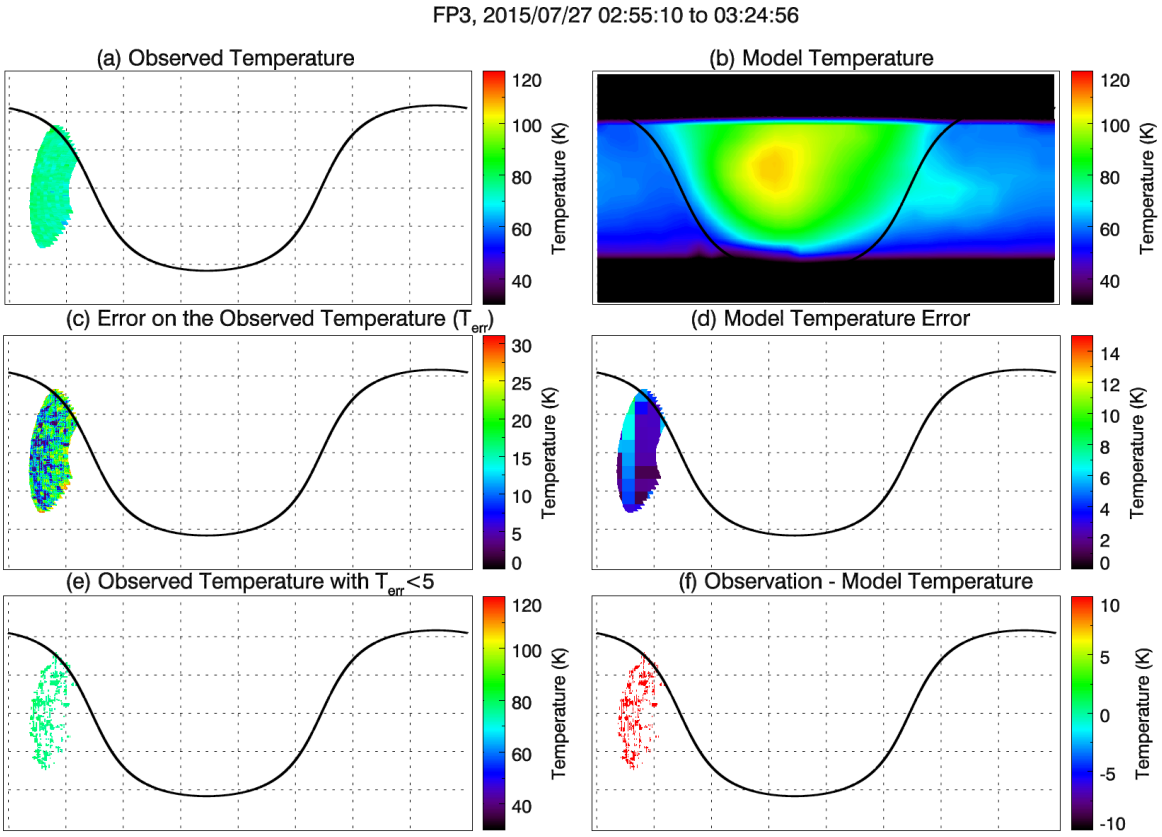
FP3, 2015/07/27 02:55:10 to 03:24:56
(a) Observed Temperature
(b) Model Temperature
(c) Error on the Observed Temperature (T_err)
(d) Model Temperature Error
(e) Observed Temperature with T_err<5
(f) Observation - Model Temperature
Temperature (K)

233

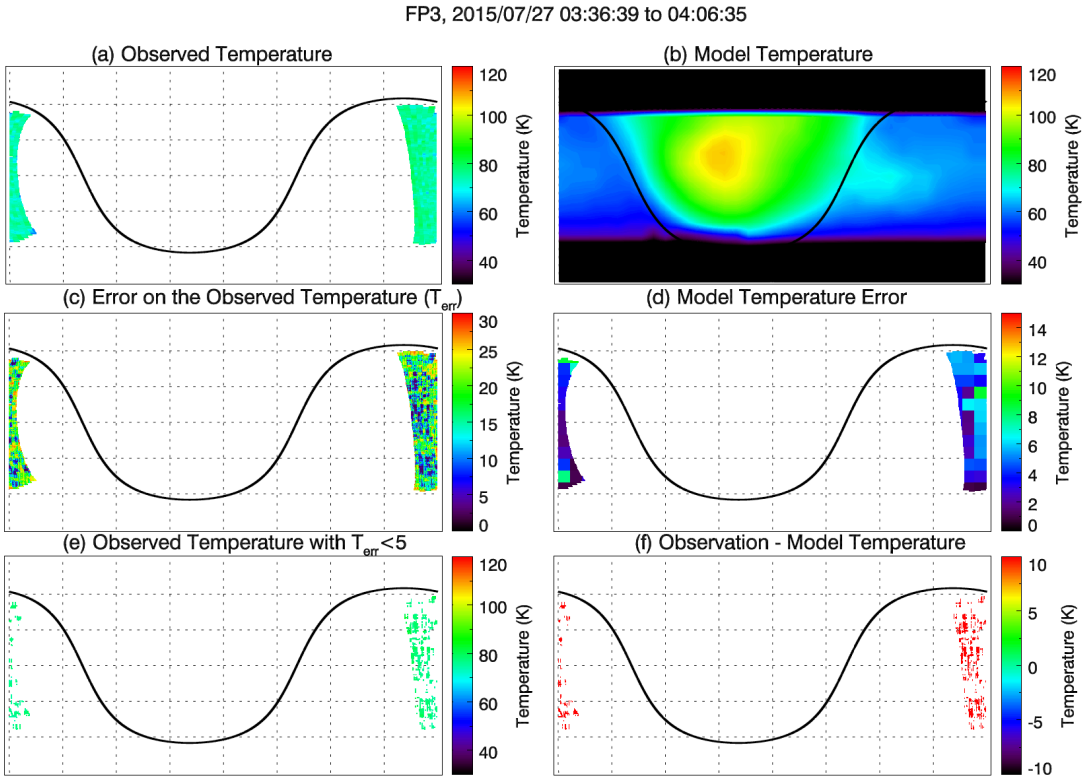
FP3, 2015/07/27 03:36:39 to 04:06:35
(a) Observed Temperature
(b) Model Temperature
(c) Error on the Observed Temperature (T_err)
(d) Model Temperature Error
(e) Observed Temperature with T_err<5
(f) Observation - Model Temperature
Temperature (K)

234
235

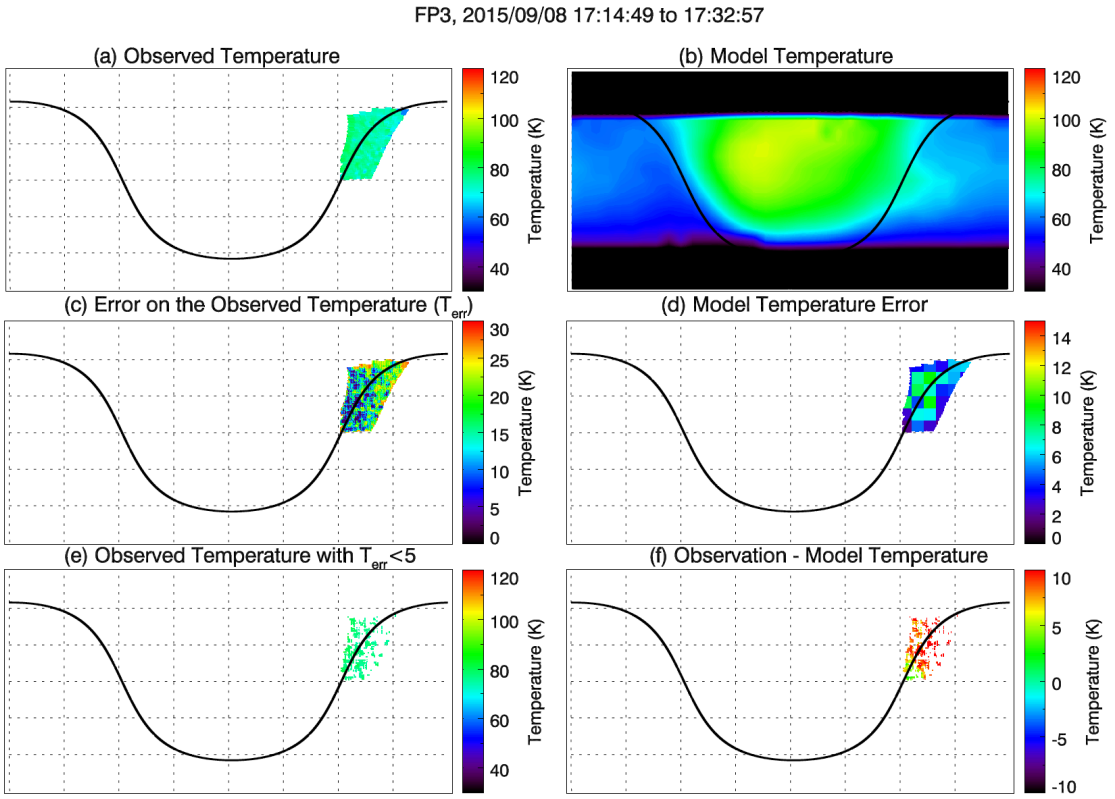
FP3, 2015/09/08 17:14:49 to 17:32:57
(a) Observed Temperature
(b) Model Temperature
(c) Error on the Observed Temperature (T_{err})
(d) Model Temperature Error
(e) Observed Temperature with T_{err}<5
(f) Observation - Model Temperature
Temperature (K)

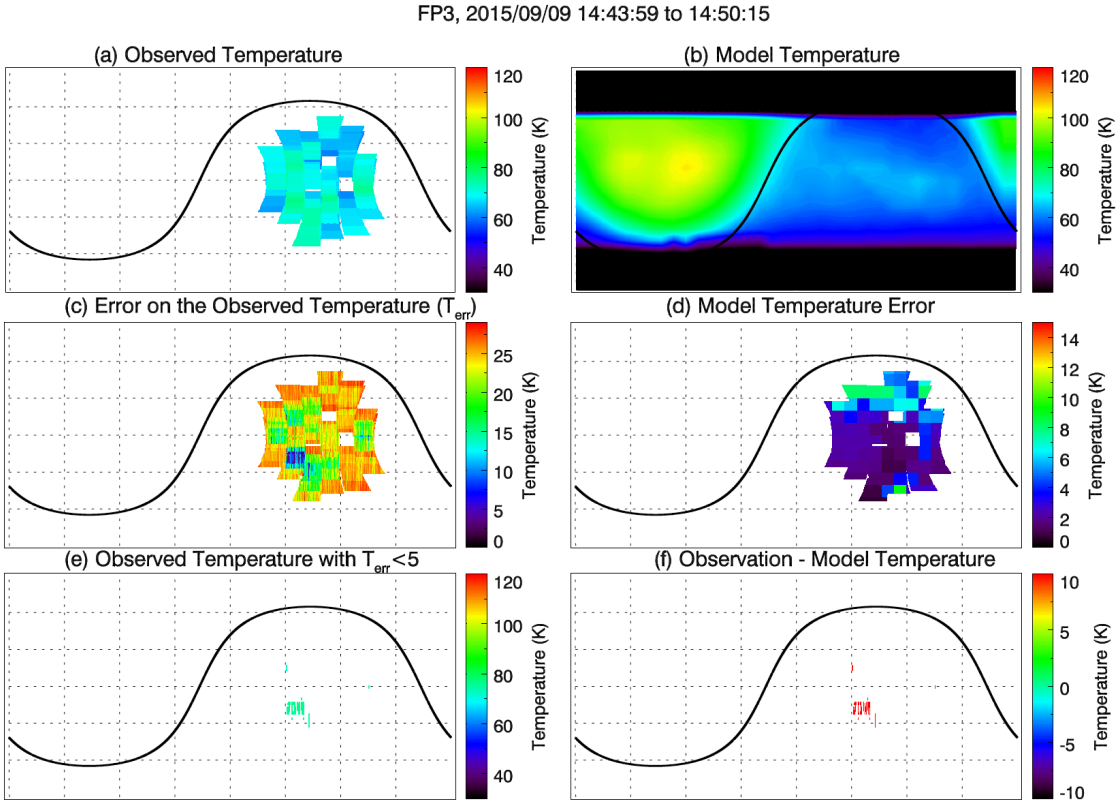
FP3, 2015/09/09 14:43:59 to 14:50:15
(a) Observed Temperature
(b) Model Temperature
(c) Error on the Observed Temperature (T_{err})
(d) Model Temperature Error
(e) Observed Temperature with T_{err}<5
(f) Observation - Model Temperature
Temperature (K)

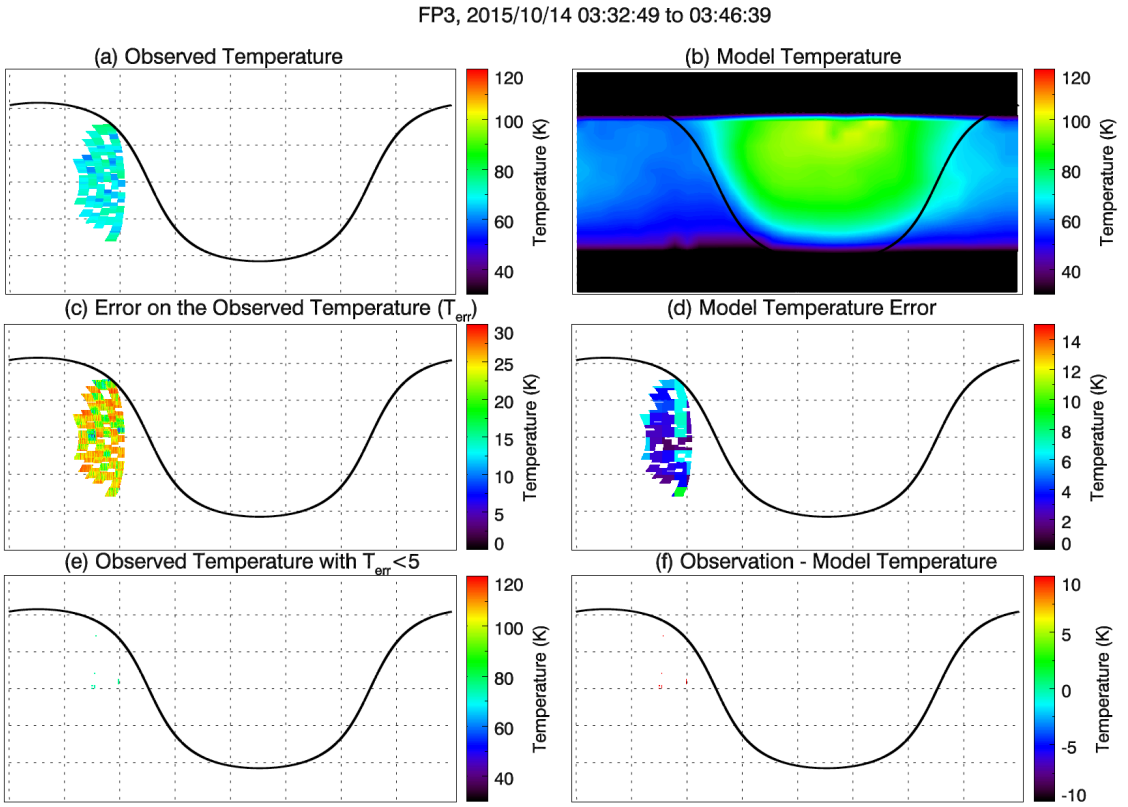
FP3, 2015/10/14 03:32:49 to 03:46:39
(a) Observed Temperature
(b) Model Temperature
(c) Error on the Observed Temperature (T_err)
(d) Model Temperature Error
(e) Observed Temperature with T_err<5
(f) Observation - Model Temperature
Temperature (K)

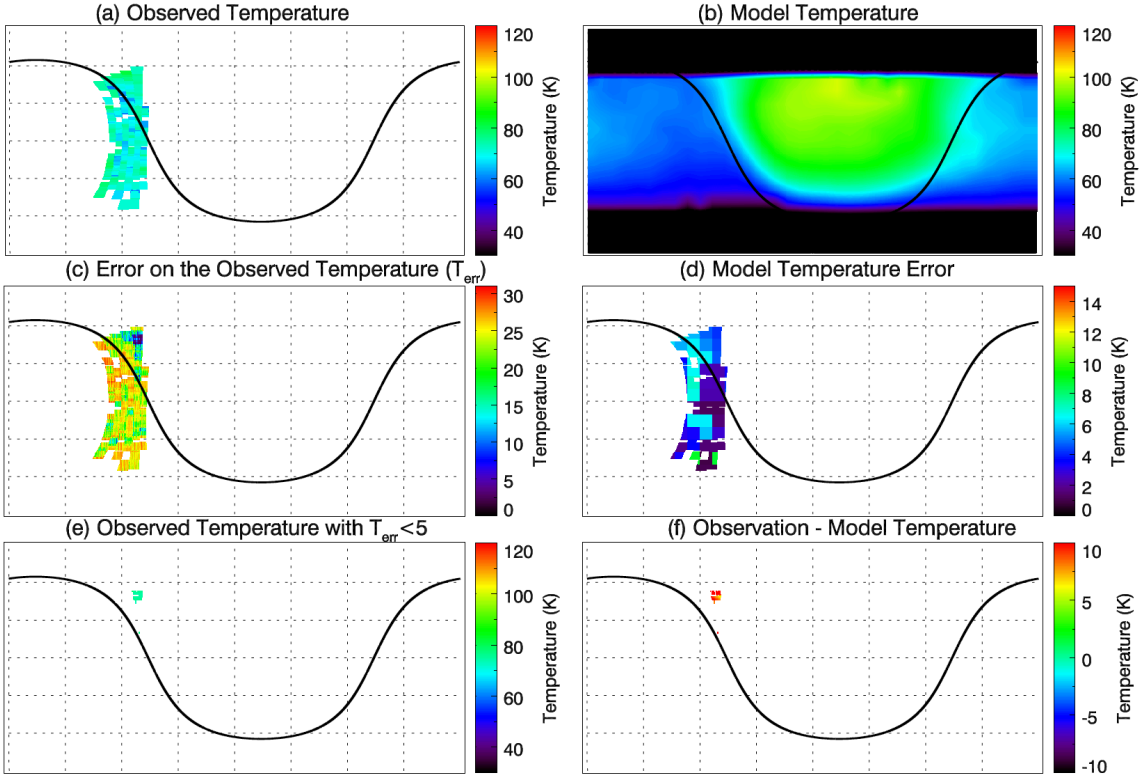
FP3, 2015/10/14 03:58:56 to 04:14:38
(a) Observed Temperature
(b) Model Temperature
(c) Error on the Observed Temperature (T_err)
(d) Model Temperature Error
(e) Observed Temperature with T_err<5
(f) Observation - Model Temperature
Temperature (K)

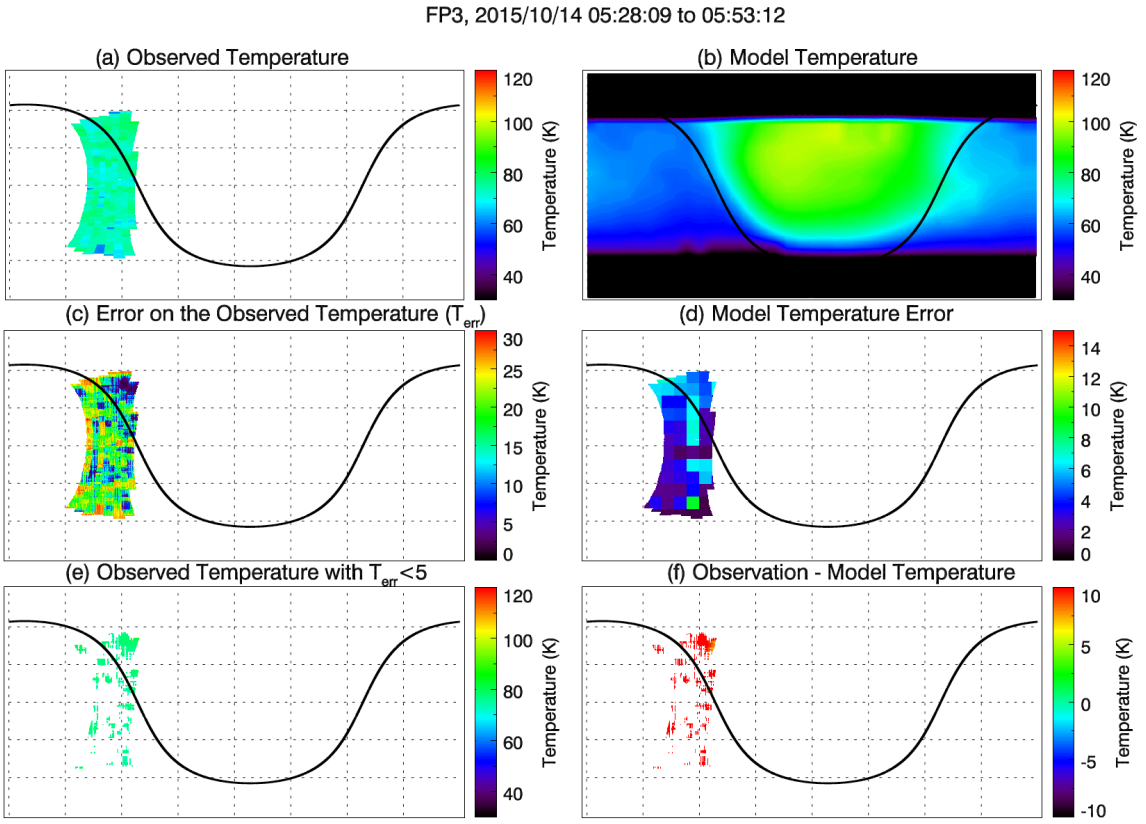
FP3, 2015/10/14 05:28:09 to 05:53:12
(a) Observed Temperature
(b) Model Temperature
(c) Error on the Observed Temperature (T_err)
(d) Model Temperature Error
(e) Observed Temperature with T_err<5
(f) Observation - Model Temperature
Temperature (K)

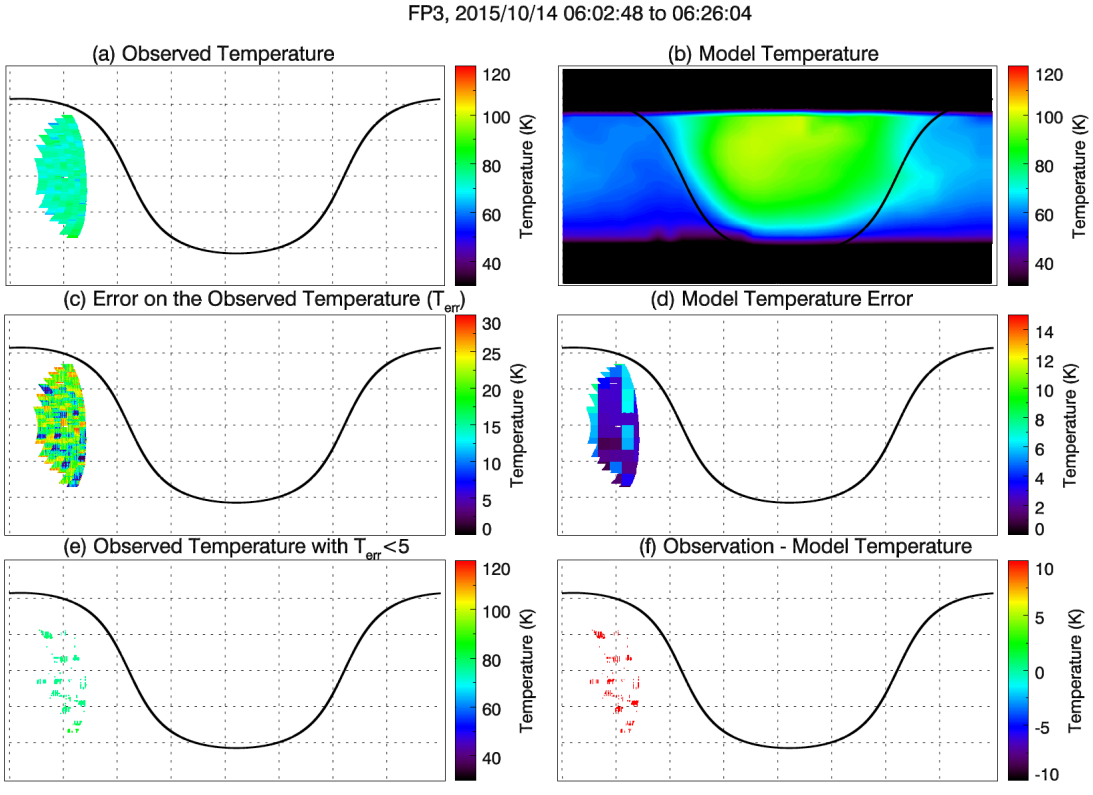
FP3, 2015/10/14 06:02:48 to 06:26:04
(a) Observed Temperature
(b) Model Temperature
(c) Error on the Observed Temperature (T_err)
(d) Model Temperature Error
(e) Observed Temperature with T_err<5
(f) Observation - Model Temperature
Temperature (K)

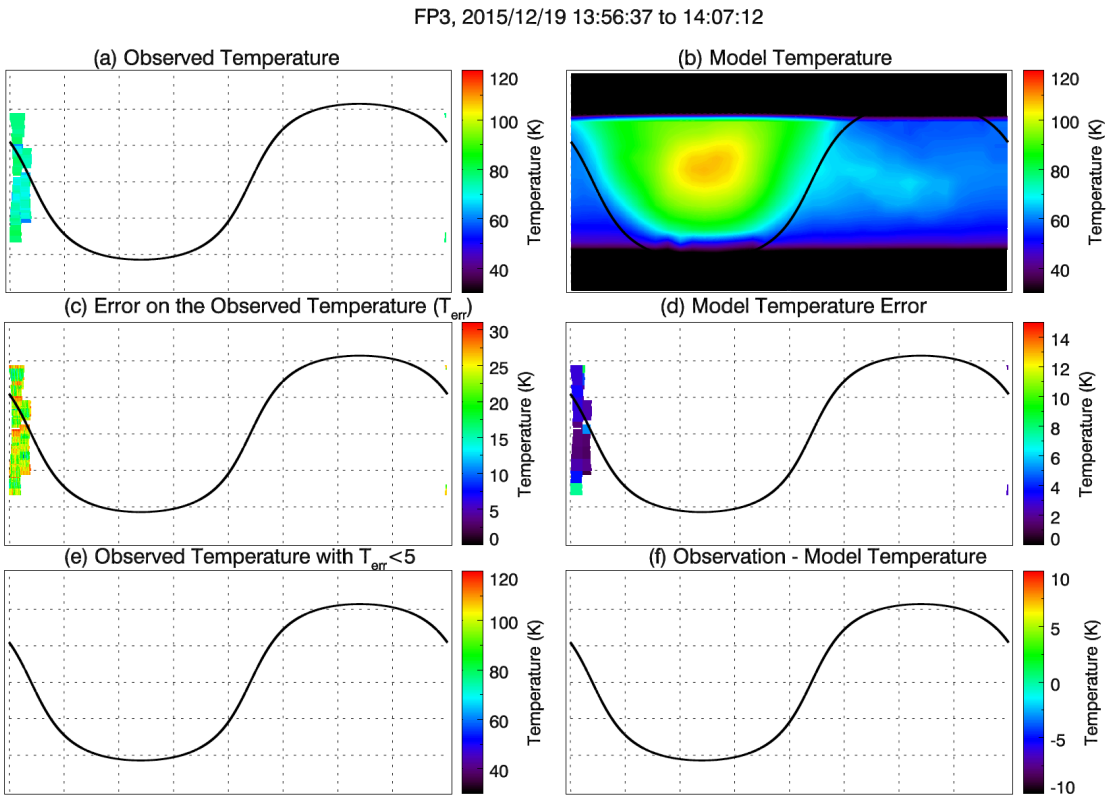
FP3, 2015/12/19 13:56:37 to 14:07:12
(a) Observed Temperature
(b) Model Temperature
(c) Error on the Observed Temperature (T_err)
(d) Model Temperature Error
(e) Observed Temperature with T_err<5
(f) Observation - Model Temperature
Temperature (K)

246

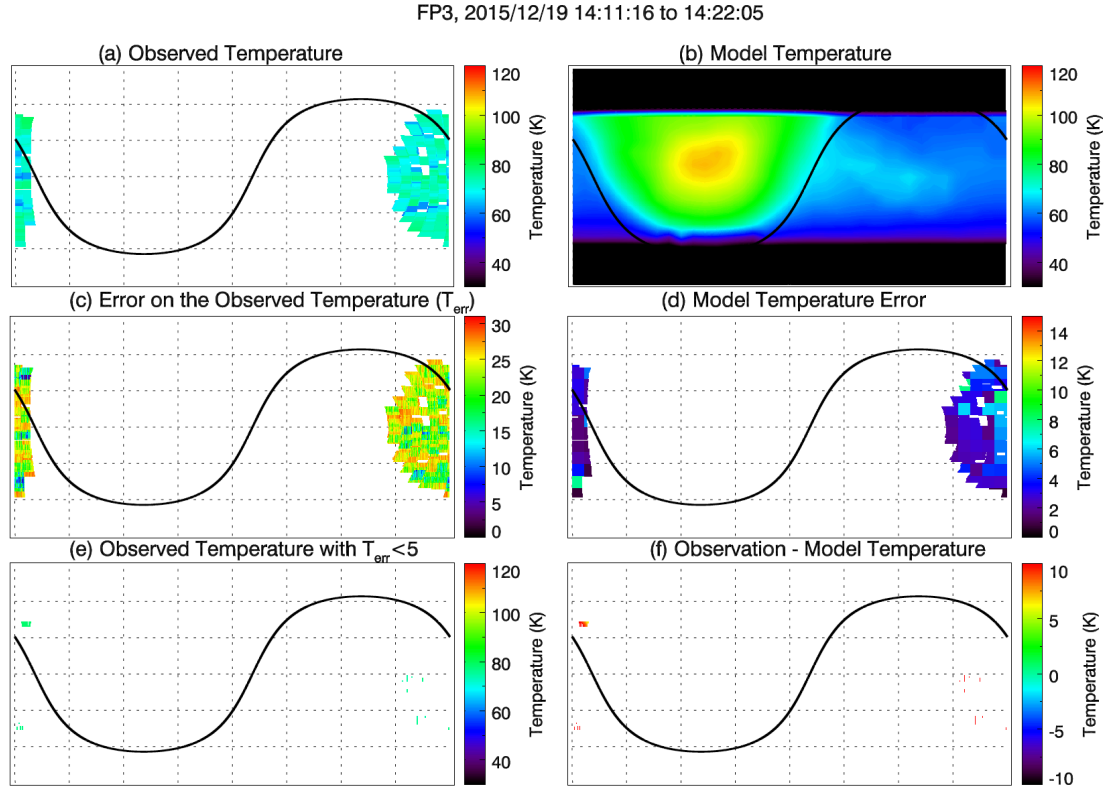
FP3, 2015/12/19 14:11:16 to 14:22:05
(a) Observed Temperature
(b) Model Temperature
(c) Error on the Observed Temperature (T_err)
(d) Model Temperature Error
(e) Observed Temperature with T_err<5
(f) Observation - Model Temperature
Temperature (K)

247

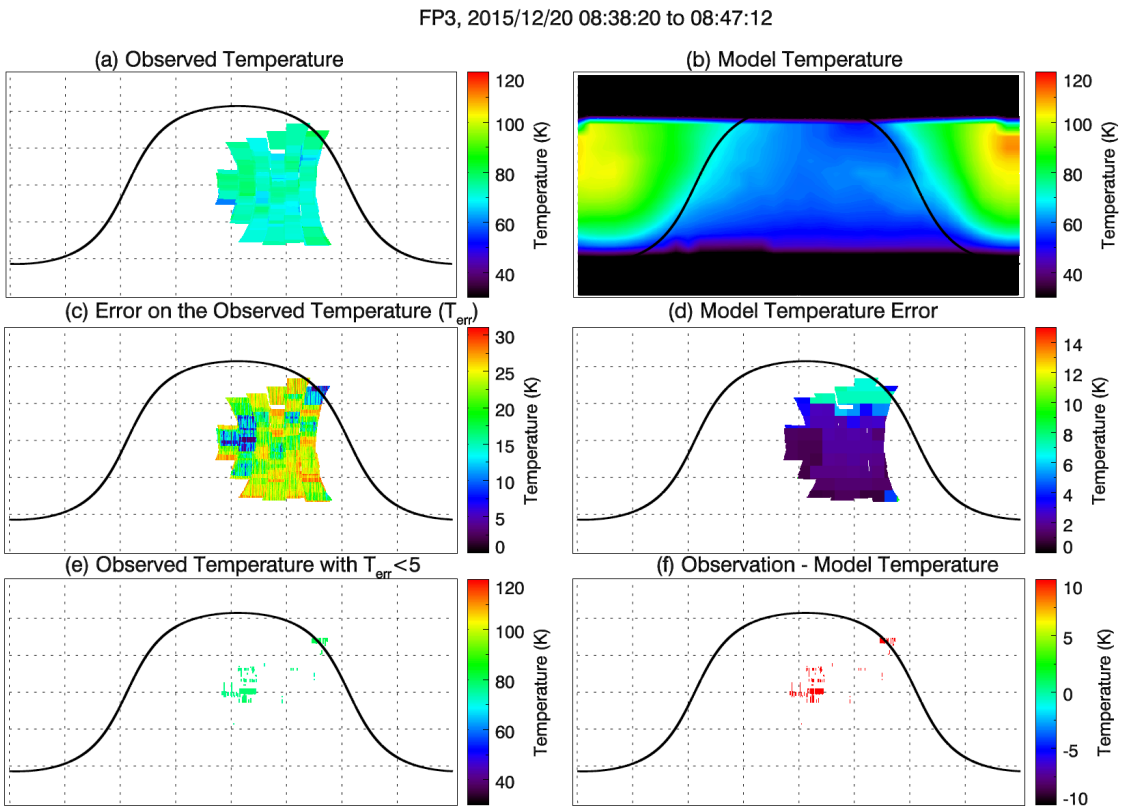
FP3, 2015/12/20 08:38:20 to 08:47:12
(a) Observed Temperature
(b) Model Temperature
(c) Error on the Observed Temperature (T_err)
(d) Model Temperature Error
(e) Observed Temperature with T_err<5
(f) Observation - Model Temperature
Temperature (K)

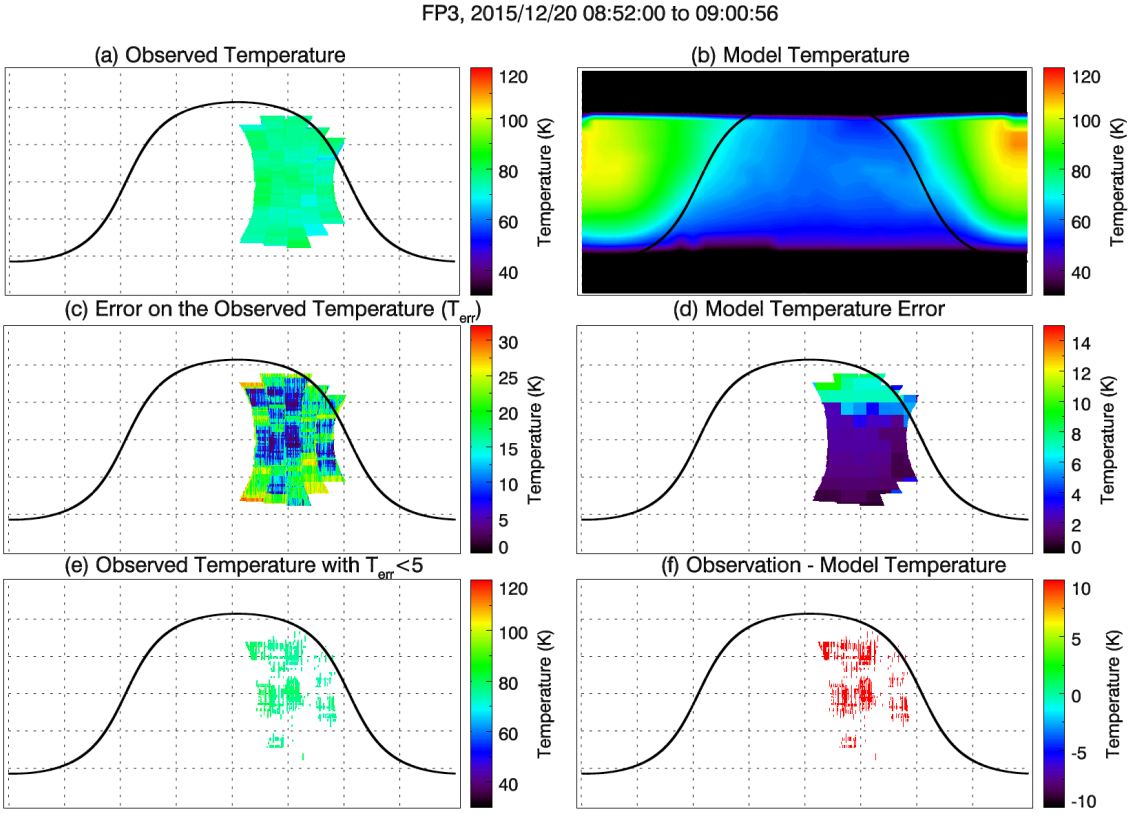
FP3, 2015/12/20 08:52:00 to 09:00:56
(a) Observed Temperature
(b) Model Temperature
(c) Error on the Observed Temperature (T_err)
(d) Model Temperature Error
(e) Observed Temperature with T_err<5
(f) Observation - Model Temperature
Temperature (K)

Figure 3 – Maps of the observed and predicted temperature for each observation epoch for FP3 observations. The detector, and start/end time of each observation are given. The left-hand-side show maps of the observed temperature, the error on that observed temperature and only observed temperatures that have an error <5 K. The right-hand-side show predicted model temperatures at the epoch of the observation, with their error. The bottom right-hand-side plot shows the difference in the observed and modeled temperatures for bins where the observed temperatures have an error <5 K. The maps have the same coordinate system as Figure 1 and 2, i.e. 360 to 0° W (left to right) longitude and 90° S to 90° N (bottom to top) latitude.

3 Results

The temperatures derived from CIRS' FP1 and FP3 observations are given in the top-right panel in Figures 2 and 3 respectively. The temperatures are largely consistent with literature values (e.g. Filacchione et al., 2016 who found daytime temperatures between ~88 and 140 K). The observation times indicated on these figures can be used to cross-reference with Table S1 for more information of the geometry of each encounter.

Early in the mission (between 2007 and early 2012) Dione experienced a number of solar eclipses; the time and duration of these eclipses are included in the seasonal model. For the eclipse to effect the surface temperatures of Dione observed it must occur when the Saturn-facing hemisphere (apex at 0° W) would otherwise be sunlit, and close to the observation time (i.e. the day before the nighttime observation). The only observation that meets these requirements occurred on 04/06/2010, the effect is clearly seen by the cooler modeled daytime temperatures at this epoch compared to others of the same hemisphere taken at a different time (Figure 2).

The errors on the FP3 spectra are much larger than that of FP1, this is expected since the wavelength range of the FP1 detector makes it more sensitive to low-temperature emission. This can be clearly seen in the errors on the derived surface temperatures: FP1 temperature errors are much lower than those of FP3, and in some instances the error on the FP3 spectra are so large the derived surface temperature should be treated with caution. In order to see the most reliable surface temperatures, maps of surface temperatures with an error of <5 K are also given in Figures 2 and 3 (bottom left panel). As these maps show very few of the FP3 surface temperatures fulfill this requirement, but most FP1-derived surface temperatures do. This means that the FP3 temperatures are best used for looking for atypical high surface temperatures, but small temperature increases (<5 to 10 K) from those predicted by the seasonal models shouldn't be automatically considered to be evidence of activity.

4 Discussion

The modeled surface temperatures given in Figures 2 and 3 vary across Dione (top right panel). Some epochs experience eclipse cooling (indicated in Table S1), these observations had an eclipse ending between 7 and 18 hours prior to the start of the observation. The effect of these eclipses on the observed temperature is expected to be minimal. For example, assuming an albedo of 0.55, a thermal inertia of 5 (25) MKS and an eclipse with a the same local time as that on 2010/04/07 then the difference between the eclipse and no-eclipse model predicted surface temperatures have a maximum temperature difference of 30 (15) K, but return to a difference of

<1 K within two (six) hours. Surface temperature differences observed in Figures 2 and 3 are caused by the change in surface properties, notably the higher albedo of Dione's leading hemisphere (which results in lower temperatures) and the high thermal inertia "PacMan" region on Dione's leading hemisphere (which results in lower daytime and warmer nighttime temperatures).

Despite these variations in Dione's surface temperature a simple visual inspection of its nighttime surface temperatures derived from CIRS observations (top right panel in Figures 2 and 3) shows that no discrete regions of notably high heat flow than their surroundings (indicative of activity) are observed. The FP3 results are particularly important in this regard, since they have a higher spatial resolution than FP1, and would be sensitive to high temperatures (>65 K). So it doesn't matter too much than the FP3 results are noisy, because this is simply in keeping with the lack of discovery of small regions of high temperature.

The observed and the predicted temperatures do not agree perfectly, but do agree to typically to within ±5 K for FP1, and ±10 K for FP3. This indicates that the surface thermophysical properties used are not perfectly correct but do provide a reasonable estimate of Dione's surface properties. The surface temperatures derived from the FP1 observations are less erroneous than that of FP3, and show the derived surface temperatures are largely cooler than those predicted, particularly in the southern hemisphere. Such a discrepancy maybe caused by assuming an albedo that was too low, or a thermal inertia that was too high, as both these would lead to warmer nighttime surface temperatures. However, the more likely culprit is thermal inertia since it influences nighttime emission more significantly: a higher thermal inertia surface is better able to retain its daytime heating into the night. Interestingly the surface temperatures derived from FP3 observations appear to display the opposite trend: they are warmer than those predicted. However, further interpretation isn't possible because the errors on the derived FP3 surface temperatures are large. Given the reasonable agreement between the observed and predicted surface temperatures it is concluded that no regions of high heat flow consistent with activity are observed by CIRS on Dione.

In the absence of any observed activity we set limits for the maximum temperature of a 50, 100 and 200 km^2 hotspots that could exist on Dione and remain undetected. The size selected for the hotspot was somewhat arbitrary, we chose values close to 100 km^2 since it was consistent with similar work on Europa (Rathbun et al., 2010). It is roughly equivalent to 1° by 1° latitude/longitude bin at Dione's equator. To find the upper limit of undetected hotspot temperature we first determined the upper-limit of passive emission for each observation. We assume it to be the sum of the (previously derived) best-fitting blackbody temperature and two times its error (i.e. the maximum observed temperature including the 2-sigma error). To prevent observations with large errors skewing the results we limit the observations to those with <5 K error. This could be expanded to also use observations with larger errors (mostly FP3) by using the predicted modeled temperature for the passive emission instead, however we found that good surface coverage was achieved without having to take this extra step.

We then added a radiance equivalent to a hotspot at a given size and temperature to the originally observed radiance, producing a new elevated radiance. The best-fitting blackbody temperature of this new radiance was then found (using the fitting method described previously). We increased

the temperature of the hotspot (T_H) until the new derived temperature was greater than the upper-limit of the passive temperature. When this occurred that hotspot temperature was assumed for the upper-limit. We then combined all of these upper-limits to form the map in Figure 4. In regions of overlapping observations the lowest hotspot limit was used. The power of these hotspots was then calculated using T_H, their area and the Stefan–Boltzmann law.

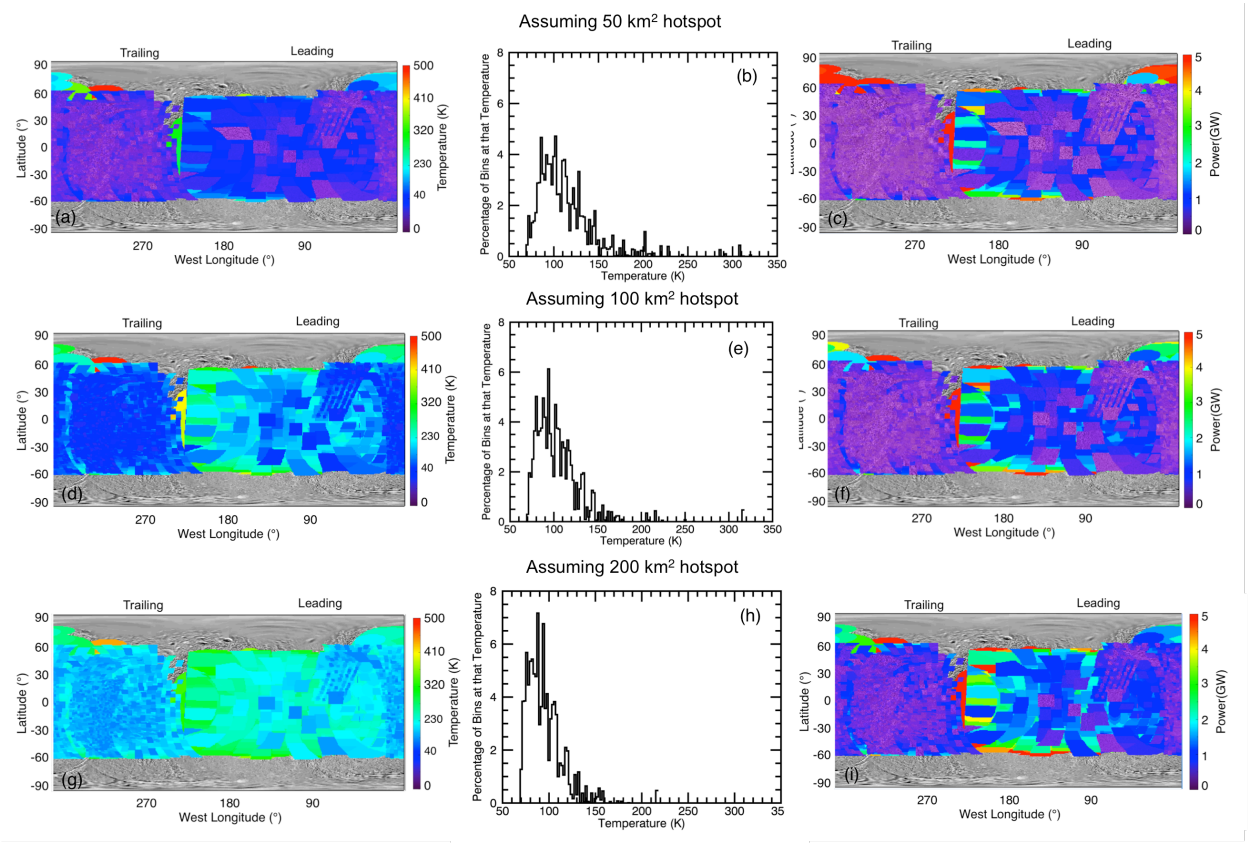

Figure 4 – Details of the upper-limits for a 50, 100 and 200 km^2 hotspot that could exist on Dione and not be detected in this work. Panels a,d,g show the maximum temperature of a hotspot that could exist on Dione and have remained undetected in this work. Panels b,e,h show the maximum power of a hotspot that could exist on Dione and have remained undetected in this work. Panels c,f,I show histograms of the maximum temperature a hotspot could have and remain undetected in this study.

The hotspot upper-limit temperatures are mapped and compiled as a histogram in Figure 4. The figure shows the hotspot temperatures are mostly between ~60 and 170 K. The expected trend of larger hotspots compensating for their size by having a lower temperatures is clearly observed in the figure. The mean and standard deviation of the upper-limit hotspot temperature for a 50, 100 and 200 km^2 hotspot respectively are: 117.1±47.2 K, 104.8±27.7 K and 95.4±19.5 K. The figure also shows that this balance between temperature and size also results in the predicted power of the undetected hotspots being similar, despite the size of the hotspot. The hotspot temperatures for a 50, 100 and 200 km^2 hotspot correspond to endogenic emissions of: 1.07, 0.68 and 0.47

GW respectively. If endogenic emission was occurring at this level then the implications would be exciting, but its worth noting this is order of magnitudes lower than the 5.8 to 15.8 GW of endogenic emission observed from Enceldaus (Spencer et al., 2006; Howett et al., 2011).

5 Conclusions

We have used Cassini CIRS FP1 and FP3 observations of Dione's surface to map its nighttime surface temperatures. The derived surface temperatures are largely consistent with those expected from seasonal models of Dione's surface temperature, and show no evidence of discrete regions of high heat flow consistent with endogenic activity. Thus we conclude we see no evidence for activity on Dione in these observations. Using these data we set an upper limit of the mean temperature of a single undetected 50, 100 or 200 km^2 hotspot on Dione to be 117.1±47.2 K, 104.8±27.7 K and 95.4±19.5, equivalent to endogenic emission of 1.07, 0.68 and 0.47 GW respectively

Acknowledgments

We would like to thank NASA's Cassini Data Analysis plan for their funding of this work (NNX13AH84G). All CIRS data analyzed in this work is available in the Planetary Data System Archive (https://pds-rings.seti.org/cassini/cirs/).

References

Burch, J.L., J. Goldstein, W.S. Lewis, D.T. Young, A.J. Coates, M.K. Dougherty and N. André (2007). Tethys and Dione as sources of outward-flowing plasma in Saturn's magnetosphere. *Nature 447*, 833-835, doi: 10.1038/nature05906.

Buratti, B.J., S.P. Faulk, J. Mosher, K.H. Baines, R.H. Brown, R.N. Clark and P.D. Nicholson (2011), Search for and limits on plume activity on Mimas, Tethys, and Dione with the Cassini Visual Infrared Mapping Spectrometer (VIMS) (2011), *Icarus 214*, 534-540, doi: 10.1016/j.icarus.2011.04.030.

Buratti, B.J., C. J. Hansen, A. R. Hendrix, L. W. Esposito, J. A. Mosher (2018), The Search for Activity on Dione and Tethys with Cassini VIMS and UVIS, *Journal of Geophysical Research Submitted*.

Clark, R.N., J.M. Curchin, R. Jaumann, D.P. Cruikshank, R.H. Brown, T.M. Hoefen, K. Stephan, J.M. Moore, B.J. Buratti, K.H. Baines, P.D. Nicholson and R.M. Nelson (2008). Compositional mapping of Saturn's satellite Dione with Cassini VIMS and implications of dark material in the Saturn system. *Icarus 193*, 372-386, doi: http://dx.doi.org/10.1016/j.icarus.2007.08.035.

406 Dougherty, M.K., K.K. Khaurana, F.M. Neubauer, C.T. Russell, J. Saur, J.S. Leisner and M.E.
407 Burton (2006). Identification of a Dynamic Atmosphere at Enceladus with the Cassini
408 Magnetometer, *Science 311*, 1406-1409, doi:10.1126/science.1120985.
409
410 Flasar, F.M., V.G. Kunde, M.M. Abbas, R.K. Achterberg, P. Ade, A. Barucci, B. Bézard, G.L.
411 Bjoraker, J.C. Brasunas, S.B. Calcutt, R. Carlson, C.J. Césarsky, B.J. Conrath, A.
412 Coradini, R. Courtin, A. Coustenis, S. Edberg, S. Edgington, C. Ferrari, T. Fouchet, D.
413 Gautier, P.J. Gierasch, K. Grossman, P. Irwin, D.E. Jennings, E. Lellouch, A.A.
414 Mamoutkine, A. Marten, J.P. Meyer, C.A. Nixon, G.S. Orton, T.C. Owen, J.C. Pearl, R.
415 Prangé, F. Raulin, P.L. Read, P.N. Romani, R.E. Samuelson, M.E. Segura, M.R.
416 Showalter, A.A. Simon-Miller, M.D. Smith, J.R. Spencer, L.J. Spilker and F.W. Taylor
417 (2004). Exploring the Saturn System in the Thermal Infrared: The Composite Infrared
418 Spectrometer, *Space Science Review 115,* 169-297, doi: 10.1007/s11214-004-1454-9.
419
420
421 Filacchione, G., E. D'Aversa, F. Capaccioni, R.N. Clark, D.P. Cruikshank, M. Ciarniello, P.
422 Cerroni, G. Bellucci, R.H. Brown, B.J. Buratti, P.D. Nicholson, R. Jaumann, T.B.
423 McCord, C. Sotin, K. Stephan, C.M. Dalle Ore (2016), Saturn's icy satellites investigated
424 by Cassini-VIMS. IV. Daytime temperature maps, Icarus 271, 292-313, doi:
425 10.1016/j.icarus.2016.02.019.
426
427 Goguen, J.D., B.J. Buratti, R.H. Brown, R.N. Clark, P.D. Nicholson, M.M. Hedman, R.R.
428 Howell, C. Sotin, D.P. Cruikshank, K.H. Baines, K.J. Lawrence, J.R. Spencer and D.G.
429 Blackburn (2013), The temperature and width of an active fissure on Enceladus measured
430 with Cassini VIMS during the 14 April 2012 South Pole flyover, *Icarus 226*, 1128-1137,
431 doi:10.1016/j.icarus.2013.07.012.
432
433 Hansen, C.J., L. Esposito, A.I.F. Stewart, J. Colwell, A. Hendrix, W. Pryor, D. Shemansky and
434 R.West (2006), Enceladus' Water Vapor Plume, *Science 311*, 1422-1425, 2006.
435
436 Howett, C.J.A., J.R. Spencer, J. Pearl and M. Segura (2010), Thermal inertia and bolometric
437 Bond albedo values for Mimas, Enceladus, Tethys, Dione, Rhea and Iapetus as derived
438 from Cassini/CIRS measurements, *Icarus, 206*, 573-593, doi:
439 10.1016/j.icarus.2009.07.016.
440
441 Howett, C.J.A., J.R. Spencer, J. Pearl and M. Segura (2011), High heat flow from Enceladus'
442 South Polar Region, *Journal of Geophysical Research 116*, E03003,
443 doi:10.1029/2010JE003718.
444

Howett, C.J.A., J.R. Spencer, T. Hurford, A. Verbiscer and M. Segura (2014), Thermophysical property variations across Dione and Rhea, *Icarus 241*, 239-247, doi: 10.1016/j.icarus.2014.05.047.

Nelder, J.A. and Mead, R. (1965). A Simplex Method for Function Minimization, *Computer Journal 7*, 308-313.

Porco, C.C., P. Helfenstein, P.C. Thomas, A. P. Ingersoll, J. Wisdom, R. West, G. Neukum, T. Denk, R. Wagner, T. Roatsch, S. Kieffer, E. Turtle, A. McEwen, T. V. Johnson, J. Rathbun, J. Veverka, D. Wilson, J. Perry, J. Spitale, A. Brahic, J. A. Burns, A. D. Del Genio, L. Dones, C. D. Murray and S Squyres (2006), Cassini Observes the Active South Pole of Enceladus, *Science, 311,* 1393–1401, doi:10.1126/science.1123013.

Rathbun, J.A., N.J. Rodriguez and J.R. Spencer (2010), Galileo PPR observations of Europa: Hotspot detection limits and surface thermal properties, Icarus 210, 763-769, doi: 10.1016/j.icarus.2010.07.017.

Roatsch, T., M. Wählisch, B. Giese, A. Hoffmeister, K-D Matz, F. Scholten, A. Kuhn, R. Wagner, G. Neukum, P. Helfenstein and C.C. Porco (2008), High-resolution Enceladus atlas derived from Cassini-ISS images, *Planetary and Space Science 56*, 109-116, doi: 10.1016/j.pss.2007.03.014.

Roatsch, Th., R. Jaumann, K. Stephan and P.C. Thomas (2009), 'Cartographic Mapping of the Icy Satellites Using ISS and VIMS Data in Saturn from Cassini-Huygens, Editors M.K. Doughterty, L.W. Esposito and S.M. Krimigis, *763–781,* Springer Press, doi:10.1007/978-1-4020-9217-6_24

Rymer, A.M., B.H. Mauk., T.W. Hill., C. Paranicas, D.G. Mitchell, A.J. Coates and D.T. Young (2008), Electron circulation in Saturn's magnetosphere, *Journal of Geophysical Research 113*, A01201, doi:10.1029/2007JA012589.

Schenk, P. D.P. Hamilton, R.E. Johnson, W.B. McKinnon, C. Paranicas, J. Schmidt, M.R. Showalter (2011), Plasma, plumes and rings: Saturn system dynamics as recorded in global color patters on its midsize icy satellites, Icarus, 211, 740-757, doi: 10.1016/j.icarus.2010.08.016.

Scipioni, F., F. Tosi, K. Stephan, G. Filachhione, M. Ciarniello, F. Capaccioni, P. Cerroni and the VIMS Team (2013), Spectroscopic classification of icy satellites of Saturn I: Identification of terrain units on Dione, Icarus 226, 1331-1349, doi: 10.1016/j.icarus.2013.08.008.

Simon, S., J. Saur, F.M. Neubauer, A. Wennmacher, M.K. Dougherty (2011), Magnetic signatures of a tenuous atmosphere at Dione, *Geophysical Research Letters 38*, L15102, doi: 10.1029/2011GL048454.

Spahn, F., J. Schmidt, N. Albers, M. Hörning, M. Makuch, M. Seiß, S. Kempf, R. Srama, V. Dikarev, S. Helfert, G. Moragas-Klostermeyer, A.V. Krivov, M. Sremčević, A.J. Tuzzolino, T. Economou and E. Grün (2006), Cassini Dust Measurements at Enceladus and Implications for the Origin of the E Ring, *Science 311*, 1416-1418, doi:10.1126/science.1121375.

Spencer, J.R. (1989) A rough-surface thermophysical model for airless planets, *Icarus 83*, 27-38, doi: 10.1016/0019-1035(90)90004-S.

Spencer, J.R., J.C. Pearl, M. Segura, F.M. Flasar, A. Mamoutkine, R. Romani, B.J. Buratti, A.R. Hendrix, L.J. Spilker and R.M.C. Lopes (2006), Cassini Encounters Enceladus: Background and the Discovery of a South Polar Hot Spot, *Science 311*, 1401-1405, doi: 10.1126/science.1121661.

Spencer, J. R., C.J.A. Howett, A.J. Verbiscer, T.A. Hurford, M.E. Segura and J.C. Pearl (2011), Observations of thermal emission from the south pole of Enceladus in August 2010, *EPSC-DPS conference*, abstract #1630.

Stephan, K., R. Jaumann, R. Wagner, R.N. Clark, D. Cruikshank, C.A. Hibbitts T. Roatsch H. Hoffmann, R.H. Brown, G. Filiacchione, B.J. Buratti, G.B. Hansen, T.B. McCord, P.D. Nicholson, K.H. Baines (2010), Dione's spectral and geological properties, Icarus 206, 631-652, doi:10.1016/j.icarus.2009.07.036

Teolis, B.D., G.H. Jones, P.F. Miles, R.L. Tokar, B.A. Magee, J.H. Waite, E. Roussos, D.T. Young, F.J. Crary, A.J. Coates, R.E. Johnson, W.-L. Tseng and R.A. Baragiola (2010). Cassini Finds an Oxygen-Carbon Dioxide Atmosphere at Saturn's Icy Moon Rhea, *Science 330*, 1813, doi: 10.1126/science.1198366.

Teolis, B.D. and J.H. Waite (2016), Dione and Rhea seasonal exospheres revealed by Cassini CAPS and INMS, *Icarus 272*, 277-289, doi: 10.1016/j.icarus.2016.02.031.

Tokar, R.L., R.E. Johnson, M.F. Thomsen, E.C. Sittler, A.J. Coates, R.J. Wilson, F.J. Crary, D.T. Young and G.H. Jones (2012). Detection of exospheric O2+ at Saturn's moon Dione, *Geophysical Research Letters 39*, L03105, doi:10.1029/2011GL050452.

Smith, B. A., L. Soderblom, R.M. Batson, P.M. Bridges, J.L. Inge, H. Masursky, E. Shoemaker, R.F. Beebe, J. Boyce, G. Briggs, A. Bunker, S.A. Collins, C. Hansen, T.V. Johnson, J.L. Mitchell, R.J. Terrile, A.F. Cook, J.N. Cuzzi, J.B. Pollack, G.E. Danielson, A.P. Ingersoll, M.E. Davies, G.E. Hunt, D. Morrison, T. Owen, C. Sagan, J. Veverka, R. Strom and V.E. Suomi (1982), A new look at the Saturn system - The Voyager 2 images, *Science 215*, 504-537, doi: 10.1126/science.215.4532.504.

Schenk P.M. and J.M. Moore (2009), Eruptive Volcanism on Saturn's Icy Moon Dione, *40th Lunar and Planetary Science Conference*, Abstract #2465.